DIFFUSION TENSOR IMAGING AT LONG DIFFUSION TIME

A Thesis
Presented to
The Academic Faculty

by

Swati Rane

In Partial Fulfillment
of the Requirements for the Degree
Doctor of Philosophy in the
The Wallace H. Coulter Department of Biomedical Engineering

Georgia Institute of Technology
August 2009

DIFFUSION TENSOR IMAGING AT LONG DIFFUSION TIME

Approved by:

Professor Xiaoping Hu,
Committee Chair
The Wallace H. Coulter Department
of Biomedical Engineering
Georgia Institute of Technology

Professor Timothy Duong, Advisor
Research Imaging Center
University of Texas Health Science Center at San Antonio

Professor Marijn Brummer
The Wallace H. Coulter Department
of Biomedical Engineering
Georgia Institute of Technology

Professor Shella Keilholz
The Wallace H. Coulter Department
of Biomedical Engineering
Georgia Institute of Technology

Professor Eric Schumacher
School of Psychology
Georgia Institute of Technology

Date Approved: 16 June 2009

To My Family,

This one is for you.

ACKNOWLEDGEMENTS

I would like to thank my advisor Professor Timothy Duong for his support, supervision and encouragement during my studies. I extend my heartfelt gratitude to Professors Xiaoping Hu and Shella Keilholz for their timely guidance during the course of my doctoral studies. I am indebted to Dr. Stuart Zola and Professor Leonard Howell at Yerkes Imaging Center, and Professor Andres Garcia at Georgia Institute of Technology for providing me with resources and the moral support to complete this work.

Thanks are due to my committee members, Professor Marijn Brummer and Professor Eric Schumacher for their valuable suggestions during my thesis proposal defense and the yearly review. I will always remember the frequent discussions, related to diffusion tensor imaging, with Drs. Xiaodong Zhang, Tsukasa Nagaoka, Yoji Tanaka and Shawn Ma. I would especially like to express my gratitude to Govind Nair for his helpful discussion on the use of long diffusion time and the use of the stimulated echo acquisition mode sequence. Keith Heberlein and Xiaodong Zhong from Siemens AG will always be remembered for their help in the pulse sequence design and hands-on scanner operation. James Champion, Wendy Williamson-Coyne and Ruth Connelly were great in arranging the experiments and animal care. Special thanks to Azma Maryem at the Athinoula Martinos Center for Biomedical Imaging, Massachusetts General Hospital, MA and Chris Edmonds, Blake Gray, Pasha and James Steinberg at the Electrical Engineering Department in Georgia Institute of Technology for helping with the testing of the surface coil and building the testing rig.

I am thankful to my colleagues, Yingxia Li, Yunmei Yan, Haiying Chen, Chunxia Li and Asamoah Bosomtwi for helpful discussions during the course of my work. I will always remember the kind company of my room-mates Laura-Lee Farrell and Luz Padro and my friends, Heena Macwan, Hanh Nguyen, Shannon Statham, Zachary Anderson, Preetesh Bhantia, Fanor Balderrama, Trish Tran, Stephanie Chen and Joy Brathwaite. A special thank you to Hanh Nguyen for accompanying me on many sleepless nights of continuous scans. I express a heartfelt gratitude towards my family for their unfaltering support throughout my graduate studies and keeping up my spirits during difficult times, especially to my brother who has been my source of inspiration for everything.

TABLE OF CONTENTS

LIST OF TABLES

LIST OF FIGURES

LIST OF SYMBOLS AND ABBREVIATIONS

δ	Duration for which the Diffusion Gradient is turned on
Δ	Interval between the Application of the two Diffusion Gradients
ϵ_1,ϵ_1,ϵ_1	Eigen Vectors of D
λ_1,λ_1,λ_1	Eigen Values of D
∇C	Concentration Gradient
γ	Gyromagnetic Ratio
b	b value
CL	Linear Anisotropy
CP	Planar Anisotropy
CS	Spherical Anisotropy
D	Appparent Diffusion Coefficient
DE	Directional Entropy
FA	Fractional Anisotropy
J	molecular flux
RA	Relative Anisotropy
t_{diff}	Diffusion Time
$T1$	Longitudinal Relxation Time
$T2$	Transverse Relaxation Time
TE	Echo Time
TR	Repetition Time
VR	Volume Ratio
x, x_0	Position of Diffusion Molecule at time equal to t and $t = 0$
ADC	Apparent Diffusion Coefficient
CC	Corpus Callosum
CNR	Contrast-to-Noise Ratio

CP	Cerebral Peduncle
CSF	Cerebro-Spinal Fluid
DSI	Diffusion Spectrum Imaging
DTI	Diffusion Tensor Imaging
DW	Diffusion Weighted
DSE	Double Spin Echo
ECM	Extra Cellular Matrix
EPI	Echo Planar Imaging
FA	Fractional Anisotropy
FACT	Fiber Assignment with Continuous Tracking
FLASH	Fast Low Angle SHot
FMT	Fast Marching Technique
GDTI	Generalized Diffusion Tensor Imaging
GM	Grey Matter
HARDI	High Angular Diffusion Imaging
IC	Internal Capsule
IVOH	Intra-Voxel Orientation Heterogeneity
MION	Magnetic Iron-Oxide Nano-compounds
LGN	Lateral Geniculate Nucleus
ODF	Orientation Distribution Function
OT	Optic Tract
PET	Positron Emission Tomography
PMI	Post Mortem Interval
ROI	Region Of Interest
SC	Superior Colliculus
SNR	Signal to Noise Ratio
SNr	Substantia Nigra

STEAM	Stimulated Echo Acquisition Mode
STEAM48	Diffusion weighted Stimulated Echo Acquisition Mode sequence with a diffusion time of 48 ms
STEAM192	Diffusion weighted Stimulated Echo Acquisition Mode sequence with a diffusion time of 192 ms
STEAM50	Diffusion weighted Stimulated Echo Acquisition Mode sequence with a diffusion time of 50 ms
STEAM200	Diffusion weighted Stimulated Echo Acquisition Mode sequence with a diffusion time of 200 ms
WM	White Matter

SUMMARY

Diffusion Tensor Imaging (DTI) is a well-established magnetic resonance technique that can non-invasively interpret tissue geometry and track neural pathways by sampling the diffusion of water molecules in the brain tissue. However, it is currently limited to tracking large nerve fiber bundles and fails to faithfully resolve thinner fibers. Conventional DTI studies use a diffusion time, t_{diff} of 30 ms - 55 ms for diffusion measurements. This work proposes the use of DTI at long t_{diff} to enhance the sensitivity of the method towards regions of low diffusion anisotropy and improve tracking of smaller fibers. The Stimulated Echo Acquisition Mode (STEAM) sequence was modified to allow DTI measurements at long t_{diff} (approximately 200 ms), while avoiding $T2$ signal loss. For comparison, DTI data was acquired using STEAM at the shorter value of t_{diff} and with the standard Double Spin Echo sequence with matched signal-to-noise ratio. This approach was tested on phantoms and fixed monkey brains and then translated to *in vivo* studies in rhesus macaques. Qualitative and quantitative comparison of the techniques was based on fractional anisotropy, diffusivity, three-phase plots and directional entropy. Tensor-field maps and probabilistic connectivity fronts were evaluated for all three acquisitions. Comparison of the tracked nerve pathways showed that fibers obtained at long t_{diff} were much longer. Further, the optic tract was tracked in *ex vivo* fixed rhesus brains for cross validation. The optic tract, traced at long t_{diff}, conformed to the well documented anatomical description, thus confirming the accuracy of tract tracing at long t_{diff}. The benefits of DTI at long t_{diff} indeed help to realize the potential of tensor based tractography towards studying neural development and diagnosing neuro-pathologies, albeit the improvement is more significant *ex vivo* than *in vivo*.

CHAPTER I

INTRODUCTION

Magnetic Resonance Imaging (MRI) is one of the most widely used medical imaging technique that offers diverse information about the human body. In addition to the highly favorably soft tissue contrast for studying anatomical details, MRI is used to study blood flow using perfusion imaging, tissue function using functional MRI, chemical composition using spectroscopy and the geometrical arrangement of tissue using Diffusion Tensor Imaging (DTI). DTI is a magnetic resonance imaging technique designed to study the neural tissue micro-structure by measuring the extent of diffusion of water molecules in the tissue. The diffusion process is obstructed by various intra-cellular and extra-cellular barriers such as the cell membranes, cell organelles and large protein molecules. In the nervous tissue, the motion of water is primarily restricted along the length of the cylindrical nerve fibers thereby, causing the diffusion process to be highly anisotropic. DTI employs this anisotropy to determine the direction of nerve fiber bundles in every voxel and delineate the neural tracts that functionally connect different regions of the brain. Current methods estimate the nerve fiber orientation by measuring the diffusion process over a short duration of about 30 ms - 55 ms. The direction of the nerve fiber is estimated in the form of a 3×3 diffusion tensor matrix. Although this duration has been shown to be sufficient in sampling all the diffusion barriers, it is conjectured that the tensor direction, being an average of all possible diffusion in the given diffusion time, can be more accurately determined if the voxel is sampled for a longer duration. This forms the hypothesis for the following Ph.D. thesis.

Chapter 2 provides a brief overview of DTI. Different DTI parameters and their clinical relevance are outlined in this section, followed by a short description of the tractography techniques to delineate neural pathways. The chapter ends with the significance of the use of DTI in studying neuro-anatomy and neuro-pathologies such as Alzheimer's Disease and dementia. DTI is not restricted to the study of the nervous tissue, but can be used to study the musculature as mentioned in this chapter. Next, limitations of DTI are explained in detail. Recent modifications that have overcome some of the disabilities of DTI are discussed. Alternate approaches that emerged in the past decade have also been outlined.

Longer diffusion times are not easily achievable with the conventional sequences that are used for diffusion weighted imaging. Chapter 3 explains the customization of the Stimulated Echo Acquisition Mode (STEAM) - Echo Planar Imaging (EPI) sequence for acquiring diffusion weighted images at higher values of diffusion time. It also shows the surface coil and the testing-rig that was built specially for acquiring images with high signal-to-noise ratio (SNR) [1]. The procedure for cross-term correction that was applied to remove the effect of unwanted gradient interactions on the diffusion measurements is described. The effect of the residual cross-terms on the calculation of Apparent Difuusion Coefficient (ADC) is elaborated here. Imaging protocols specific to the *ex vivo* and *in vivo* scans are tabulated. Experimental set-up for the conventional spin echo sequence is also explained in this chapter.

To test the hypothesis, high resolution DTI data was obtained using formalin-fixed rhesus brains and analyzed for changes in Fractional Anisotropy (FA), ADC, tensor behavior and estimation of neural connectivity (Chapter 4). Comparison with the standard spin echo sequence is also shown in this work. For analysis purposes, FA, ADC, directional entropy (DE), fast marching and line propagation techniques have been employed. After confirming that the use of long diffusion time indeed improves

---

[1] The signal to noise ratio (SNR) is equal to the ratio of the average signal intensity over the standard deviation of the noise.

DTI based tractography, the imaging protocol was translated to *in vivo* studies in rhesus macaques. Analysis of the *in vivo* experiments is explained in detail in this chapter.

Chapter 5 describes the projections of the optic tract that were studied in order to validate the results obtained using DTI at long diffusion time against the standard neural pathway, as described accurately in the literature. The optic fibers from the chiasm to the Lateral Geniculate Nucleus (LGN) and the Superior Colliculus (SC) were studied using the standard sequence at $t_{diff} = 45$ ms and with DTI at $t_{diff} = 192$ ms using the STEAM sequence.

Chapter 6 summarizes the research conducted in this study and explains in brief, the observations of the study.

CHAPTER II

DIFFUSION IMAGING BASICS

Diffusion Tensor Imaging (DTI) is a Magnetic Resonance Imaging (MRI) technique based on the random thermal motion of water molecules within the nervous tissue. This random diffusion of water molecules is restricted by various intra-cellular and extra-cellular barriers that arise within the tissue microstructure. Barriers in the form of cell membranes, cell organelles and macromolecules result in a non-uniform displacement of water molecules within a tissue compartment such as the White Matter (WM) of the brain, making the diffusion highly anisotropic. The diffusion in the WM is affected by hydration, myelination, nerve fiber density and the fiber diameter [9, 80]. On the other hand, water diffuses more uniformly in tissues like the Grey Matter (GM) , resulting in a diffusion based contrast between WM and GM. Further, in the neural WM tissue, the diffusion of water molecules is largely governed by the long cylindrical nature of the axonal fibers that make up the tissue. Therefore, an estimation of the direction of diffusion in such a structure provides an estimate of the orientation of nerve fibers. Thus, it allows researchers to determine the physical arrangement of the neural pathways on a voxel-by-voxel basis.

DTI is the only imaging technique that allows a non-invasive, high resolution study of the hard and soft tissue including deep tissue structures without affecting the on-going diffusion process. DTI output provides an estimate of the Apparent Diffusion Coefficient (ADC), the diffusion anisotropy in three-dimensional (3D) space and the direction of diffusion within the tissue. Anisotropy indices and the apparent diffusion coefficients in the different tissue compartments are clinically relevant for diagnosis of neuro-degenerative diseases. Further, the direction of diffusion serves to depict the direction of the underlying tissue structure. Therefore, DTI can be used to study any modification in the nerve fiber pathway due to a neuropathology such as a tumor.

2.1 Diffusion Imaging

2.1.1 Molecular Diffusion Measurement

The random thermal motion of water molecules in the nervous system can be modeled using the Fick's laws of diffusion. According to Fick's law [25], for any cell in a steady state of non-equilibrium, the motion/diffusion of water molecules from a location of higher concentration to a location of lower concentration is determined by equation (1). It describes the relation between the diffusion coefficent, D, the rate of diffusion of water, J, across a concentration gradient (difference in the higher and lower concentration), ∇C. J is also known as the molecular flux.

$$J = -D\nabla C \tag{1}$$

Using the conservation laws for mass balance, the rate of change in concentration of water molecules must be equivalent to the gradient of the molecular flux. Therefore,

$$\frac{\partial C}{\partial t} = -\nabla J \tag{2}$$

Using equation (1) in equation (2),

$$\frac{\partial C}{\partial t} = \nabla(D\nabla C) \tag{3}$$

Equation (3) can be solved using boundary conditions to determine the value of the [17] diffusion coefficient. If the concentration at $t = 0$, is considered to be a δ function, $C(x, 0) = \delta(x - x_0)$, then the solution [75] of the above equation is a Gaussian function shown below (Equation (4))

$$C(x,t) = e^{-\frac{\frac{(x-x_0)^2}{4Dt}}{4\pi D t^{3/2}}} \tag{4}$$

Now, self Probability Density Function (PDF) of a molecule can be defined as the probability of finding a molecule that was initially located at x_0 at $t = 0$, at another location x at a time t. The above Gaussian function is equivalent to the self probability density function and therefore,

$$P(x|x_0, t) = e^{-\frac{\frac{(x-x_0)^2}{4Dt}}{4\pi Dt^{3/2}}} \tag{5}$$

Einstein [17] showed that the variance of the above self PDF is a function of the diffusivity, D of the water molecules in the cell.

$$\left\langle (x - x_0)^2 \right\rangle = \int_{\infty}^{\infty} (x - x_0)^2 P(x|x_0, t) d((x - x_0)) = 6Dt \tag{6}$$

Thus, Equation (5) concludes that the D can be estimated by calculating the second moment of the self PDF of the diffusing species.

Conventionally, diffusion imaging uses two diffusion gradients that are used to make the MR output sensitive to the diffusion of water molecules (spins) in the brain tissue. The two diffusion gradients are separated by a 180° pulse, as shown in Figure 1. The first gradient introduces a net phase shift of φ_1, and the second gradient introduces a phase shift of φ_2. If the diffusion gradients were applied along Z direction, the net phase difference is given as follows

$$\varphi_1 = \gamma \int_0^{\delta} G z_1 dt = \gamma G \delta z_1$$

$$\varphi_2 = \gamma \int_{\Delta}^{\Delta+\delta} G z_2 dt = \gamma G \delta z_2$$

$$\varphi_2 - \varphi_1 = \gamma G \delta (z_2 - z_1)$$

In DTI, the total diffusion can be measured as a the sum of the magnetic moments of the individual nuclei, S, given that the initial magnetization was S_0. S can be written in terms of a PDF, just like the self PDF mentioned earlier, and the net phase shift between the spins. The PDF is given by Equation (7).

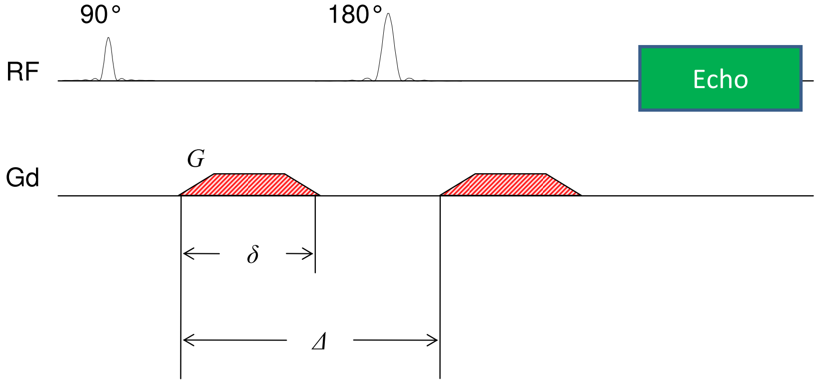

Figure 1: Representation of a Diffusion Imaging Sequence. (RF: Radio Frequency Pulse, Gd: Diffusion Gradients, δ: Duration for which the diffusion gradient is switched on, Δ: Interval between the application of the two diffusion gradients

$$P(z_1, z_2, \Delta) = \frac{1}{\sqrt{4\pi D\Delta}} e^{\frac{-(z_1-z_2)^2}{4D\Delta}} \tag{7}$$

The attenuation S in magnetization S_0, due to diffusion, can be written as

$$\frac{S}{S_0} = \int_{-\infty}^{\infty} \int_{-\infty}^{\infty} e^{i\gamma G\delta(z_1-z_2)} P(z_1, z_2, \Delta) dz_1 z_2 \tag{8}$$

Using Equation (7) in (8), gives,

$$\frac{S}{S_0} = e^{-(\gamma G\delta)^2 D\Delta} \tag{9}$$

The above equation forms the basis of the MRI signal attenuation measured due to the diffusion of water molecules.

2.1.2 Imaging Technique

As mentioned above, diffusion imaging involves measuring the diffusion of water molecules in an object under the influence of an additional pair of gradients over a preset duration. These gradients are called diffusion gradients . The extent of diffusion is reflected as the loss in signal intensity [6]. The signal intensity is measured in order to determine the effect of diffusion and is given by a simple exponential in

Equation (10). Equation 9 is slightly modified to suit a generalized diffusion weighter pulse sequence.

$$S = S_0 e^{-bD} \tag{10}$$

where

where

S = intensity of diffusion weighted image

S_0 = image intensity in the absence of any diffusion gradients

b = factor characterizing the diffusion gradients (s/mm^2) $= \gamma^2\delta^2G^2(\Delta - \delta/3)$

  γ = gyromagnetic ratio

  δ = duration for which the diffusion gradient is switched on

  G = Magnitude of diffusion gradient

  Δ = time between the application of the 2 diffusion gradients

D = apparent diffusion gradients (mm^2/s)

$t_{diff} = \Delta - \frac{\delta}{3}$

This equation applies to a 2D diffusion process. In three dimensions [65], D is represented by a 3×3, rank 2 matrix called the diffusion matrix or a tensor. Similarly, b transforms to a 3×3 matrix shown in Equation (11)

$$S = S_0 \exp - \sum_{i=1}^{n} \sum_{i=1}^{3} b_{ij} D_{ij} \tag{11}$$

where $b = \begin{pmatrix} b_{xx} & b_{xy} & b_{xz} \\ b_{yx} & b_{yy} & b_{yz} \\ b_{zx} & b_{zy} & b_{zz} \end{pmatrix}$, $D = \begin{pmatrix} D_{xx} & D_{xy} & D_{xz} \\ D_{yx} & D_{yy} & D_{yz} \\ D_{zx} & D_{zy} & D_{zz} \end{pmatrix}$.

Eigen analysis of D provides us with the principal eigen vectors - $\epsilon_1, \epsilon_2, \epsilon_3$, which depict the direction of diffusion. The principal eigen vector represents the dominant direction of diffusion and hence also the orientation of the underlying fiber bundle.

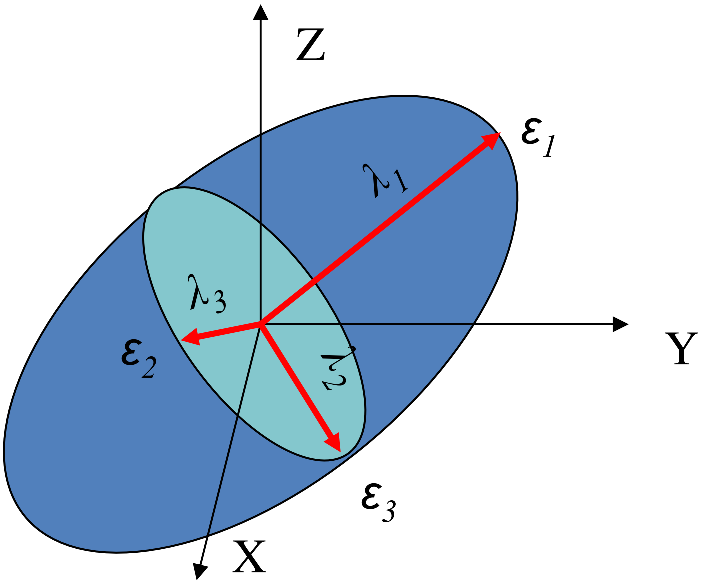

Figure 2: Diffusion Ellipsoid : The 3D diffusion in every voxel is represented by a rank 3 tensor, also represented by a diffusion ellipsoid. Eigen decomposition of the tensor matrix provides us with the three eigen values, $\lambda_1, \lambda_2, \lambda_3$, and the three principal eigen vectors, $\epsilon_1, \epsilon_2, \epsilon_3$. The prinicpal eigen vector ϵ_1 represents the dominant direction of diffusion.

The eigen values - $\lambda_1, \lambda_2, \lambda_3$ defines the extent of diffusion in the direction of the eigen vectors (Figure 2).

Since $D_{xy} = D_{yx}$, $D_{yz} = D_{zy}$ and $D_{xz} = D_{zx}$, there are six unknown variables in the D matrix. In order to solve for the values of these 6 unknowns, at least six different diffusion weighted images must be acquired, in addition to the b_0 image. b_0 image is acquired in the absence of any diffusion gradients i.e., in the absence of diffusion weighting. Typically, many more ($\gg 6$) diffusion weighted images are obtained for a more accurate estimation of the tensor orientation.

2.1.3 Characterization of Diffusion

2.1.3.1 Apparent Diffusion Coefficient (ADC):

Apparent diffusion coefficient is an intrinsic property of the tissue based on the diffusion of water in the tissue. From classic physical chemistry, diffusion coefficients are calculated over a very long time (theoretically, $t_{diff} = \infty$). The DTI measurement, however, is done over a finite time duration; therefore, D is called the apparent diffusion coefficient (ADC) and is used to characterize different tissues. For example, the value of D in healthy gray matter tissue is 0.76×10^{-3} mm^2/s. In neuro-degenerative diseases, that affect the gray matter, changes in D can be tracked to study brain injury [69]. Thus, D can be used as a diagnostic measure for various neuro-pathologies.

2.1.3.2 Fractional Anisotropy (FA):

Fractional Anisotropy (FA) [8] is another important parameter obtained from diffusion tensor imaging. FA is a measure of the fraction of the total diffusion that can be attributed to anisotropic diffusion and is calculated from the eigen values of the diffusion matrix by using Equation 12. Typical FA values in the GM and WM of humans are 0.15 and 0.65 respectively [43, 7].

$$FA = \sqrt{\frac{(\langle\lambda\rangle - \lambda_1)^2 + (\langle\lambda\rangle - \lambda_2)^2 + (\langle\lambda\rangle - \lambda_3)^2}{(\langle\lambda\rangle)^2}} \tag{12}$$

$\langle\lambda\rangle = \frac{\lambda_1+\lambda_2+\lambda_3}{3}$ is nothing but the apparent diffusion coefficient, D.

2.1.3.3 Relative Anisotropy (RA) :

Relative anisotropy [8] is another popular measure of diffusion anisotropy.

$$RA = \sqrt{\frac{Var(\lambda_i)}{\langle\lambda\rangle}} \tag{13}$$

FA and RA are widely used as diagnostic measures in assessing injuries and for studying diffusion properties of different tissue types. However, it has been shown that RA is more susceptible to noise and that FA maps have a better SNR and Contrast-to-Noise Ratio (CNR) [1] relative to RA maps [24].

---

[1] Contrast-to-Noise Ratio is the difference in signal intensities in two regions with respect to the image noise level.

2.1.3.4 Volume Ratio (VR)

Volume Ratio depicts the ratio of the ellipsoidal volume to the volume of the sphere of radius $\langle\lambda\rangle$ (Equation 14). VR has the highest standard deviation [87] at low SNR and tends to be over-estimated during diffusion measurements and is seldom used.

$$VR = \frac{\lambda_1\lambda_2\lambda_3}{\langle\lambda\rangle^3} \tag{14}$$

2.1.3.5 Geometric Measures of Anisotropy

Geometric measures of anisotropy are used to determine the nature of diffusion as a function of the underlying tissue micro-structure [2]. Based on the eigen values obtained for the diffusion matrix, D, diffusion can be classified [83] as follows:

1. **Linear Diffusion :** When $\lambda_1 \gg \lambda_2\ \lambda_3$, the tensor is a rank one tensor and the diffusion is characterized as linear. Voxels satisfying this property comprise of highly unidirectional fibers. Linear diffusion is represented by a cigar-shaped ellipsoid. Linear diffusion (CL) is calculated as

$$CL = \frac{\lambda_1 - \lambda_2}{\lambda_1 + \lambda_2 + \lambda_3} \tag{15}$$

2. **Planar Diffusion :** Planar diffusion indicates the presence of multiple fiber orientations in the voxel and is represented by a oblate or disc-shaped ellipsoid. It is characterized by a rank 2 diffusion tensor i.e., when $\lambda_1 \approx \lambda_2 \gg \lambda_3$. Planar diffusion ($CP$) is given by the following equation -

$$CP = \frac{2(\lambda_2 - \lambda_3)}{\lambda_1 + \lambda_2 + \lambda_3} \tag{16}$$

3. **Spherical Diffusion :** Spherical diffusion (CS) is a measure of isotropic diffusion where $\lambda_1 \approx \lambda_2 \approx \lambda_3$ and is given by equation (17). Since CS represents uniform diffusion, it is represented by a sphere.

$$CS = \frac{3\lambda_3}{\lambda_1 + \lambda_2 + \lambda_3} \tag{17}$$

Figure 3 depicts the shape of the diffusion ellipsoid based on the nature of diffusion represented by CL, CP and CS.

CL	Rank 1 Tensor $\lambda_1 >> \lambda_2 \approx \lambda_3$	
CP	Rank 2 Tensor $\lambda_1 \approx \lambda_2 >> \lambda_3$	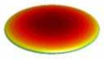
CS	Rank 3 Tensor $\lambda_1 \approx \lambda_2 \approx \lambda_3$	

Figure 3: Geometrical Interpretation of Diffusion

2.1.3.6 Directional Entropy (DE):

A directional distribution of the tensor orientations in a specific tissue regions can be calculated by using the direction of the principal eigen vectors and estimating the directional entropy [56]. For this purpose, a unit sphere is triangulated and discretized angular directions are obtained in the form of tensors through the center of the sphere and each triangular surface on the sphere. The tensors are then grouped based on the similarity in their orientation with the discretized angular directions. The eigen vectors are subsequently binned into discrete orientations corresponding to the faces of the triangulated sphere (Figure 4, Figure 5). A probability density function $p(i)$ is obtained based on the distribution of the eigen vectors and used to calculate the directional entropy.

$$DE = -\sum(p(i))\log_2(p(i)) \tag{18}$$

Directional entropy is measured over a large group of voxels for better estimation. Since entropy is a measure of chaos in the system, highly directional tissue orientation such as that found in the white matter has a much smaller DE when compared to the grey matter, where the tensor orientations are more or less randomized. It has been shown that the SNR characteristics of DE and FA are similar. DE, therefore can be used as yet another robust parameter to evaluate diffusion anisotropy [56].

2.2 Tractography

Apart from the anisotropy and diffusivity measures that can be used for diagnostic purposes, eigen analysis of the diffusion tensor provides us with a predominant direction of diffusion in the brain structure. This direction reflects the underlying tissue-geometry and thus serves as a local fiber direction in every voxel. Connecting the fiber orientation across voxels allows the delineation of nerve pathways in the brain. This is a common process of tracking fibers [49] across the brain volume. However, fiber tracking techniques can be broadly classified into two groups. Methods that use tensor information in each voxel independently, as described above, are called line propagation techniques. On the other hand, techniques that use tensor information from neighboring voxels, to minimize entropy and consequently minimize the contribution of noise, are classified as energy minimization techniques.

2.2.1 Line Propagation Techniques

These methods simply start from a seed point and follow the local tensor orientation as shown in Figure 6. One such method is Fiber Assignment with Continuous Tracking

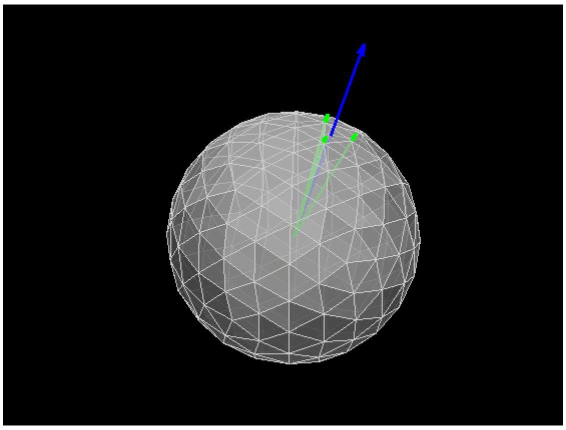

Figure 4: Sphere Triangulation

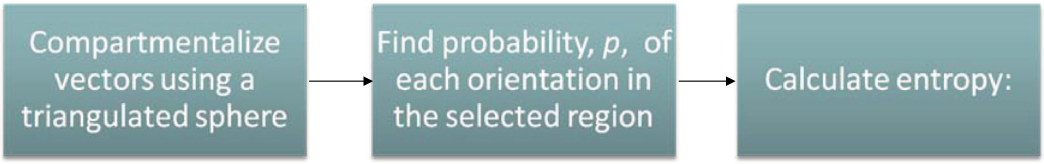

Figure 5: *DE*: The flow chart for calculating the directional entropy

(FACT) [48]. The estimated local tensor orientation may not always be translated into a accurate fiber track. For this purpose, the voxels are subdivided into sub-voxels. At every sub-voxel, a distance-averaged tensor orientation is calculated to facilitate a smoother track using interpolation. The nerve fiber being traced is terminated on the basis of FA and/or the turn angle of the fiber. The main assumption for DTI is that the diffusion process in the brain structure along any orientation is Gaussian, thus preventing the presence of sharp turns in the fiber direction. Typically the grey matter (GM) FA is around 0.15 and fiber tracking is terminated when the diffusion anisotropy drops to this value.

A significant drawback of this technique is its dependence on the information available in one voxel alone. Any error in the estimation of the tensor causes an error in the estimation of the fiber tracks and is further propagated along its length.

2.2.2 Energy Minimization Techniques

Energy minimization techniques aim to reduce the error propagation due to noise by using tensor orientation information from the adjacent voxels. Fast marching method [59] is one such energy minimization method. This method maps the extent of diffusion of water in terms of a diffusing front or a connectivity profile. The rate at which the connectivity profile propagates from one voxel to another depends on the collinearity of the principal eigen vector, ϵ_1, amongst the neighbors and the direction in which the front continues to evolve. It is similar to obtaining the contour plot of the diffusion process starting at the originating voxel [49]. The most likely path that connects any arbitrary point to the original seed point is obtained by the steepest

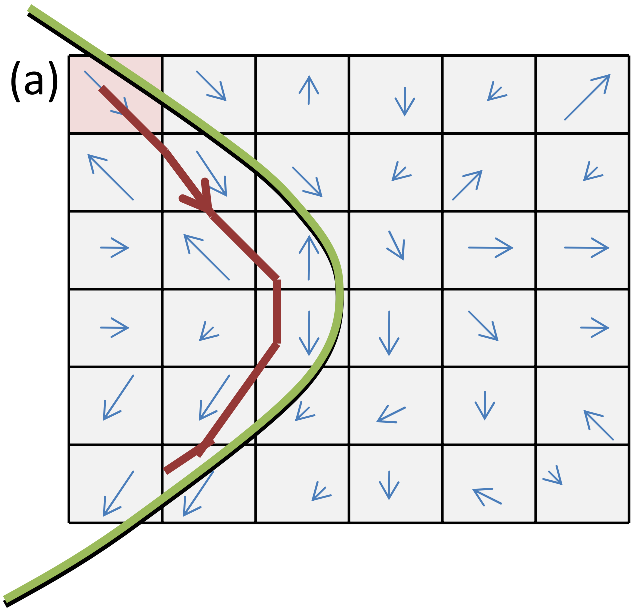

Figure 6: Simple Line Propagation: The green fiber represents the actual fiber arrangement while the fiber in red is traced by using simple line propagation technique. Voxel-by-voxel tensor orientation is shown in the background.

descent along these contour lines.

2.3 Clinical Relevance

The abundant and varied information that DTI provides is highly useful in detailed neuro-anatomical studies. For example, diffusion tensor imaging plays an important role in understanding the growth and development of the brain [67, 63, 12]. Some prominent white matter pathways such as the corpus callosum, internal capsule, longitudinal fasciculus are thin in newborns and gradually become thicker as the brain matures. Studies have shown that the ADC decreases and FA increases progressively within the first two years of brain development as white matter pathways become thicker and more compact. Brain maturation is much slower as the individual reaches adolescence [90, 51]. Presently, region-specific decrease in the FA in old age, due to the loss of nerve fibers and decreased myelination, is being studied to understand the aging process of the brain [50].

DTI also finds potential in non-invasive studies of various neuro-degenerative pathologies such as ischemia, multiple sclerosis, Alzheimer's Disease, Traumatic Brain Imaging [85] etc. DTI studies [53] have shown that patients suffering from Alzheimer's Disease show a significant decrease in the ADC in the cingulum, frontal and parietal lobes while the ADC in all other cortical regions is more or less unaffected. Additionally, FA decreased in the splenium of the corpus callosum, frontal lobe and the temporal lobe. These changes cannot be detected using conventional MRI. DTI has provided an insight into the nature of the disease and has therefore proved useful in the treatment of the disease. DTI finds similar applications in the diagnosis of multiple sclerosis, schizophrenia [34, 20] and dementia [74].

Diffusion tensor imaging is recently being used to study skeletal muscle structure. Similar to neuro-pathologies, decrease in anisotropy serves as a measure to evaluate muscle injury [89]. Muscle tissue consists of highly organized muscle fibers like the nerve fibers in the brain. Muscle injury causes a disruption of these muscle fibers, thus increasing diffusivity. Studies show that all three eigen values, λ_1, λ_2, and λ_3 increased significantly, following a muscle tear. ADC analysis in this study also revealed muscle lesions in patients with hematoma. Consistent with the nature of the injury, FA substantially decreased in the injured muscle.

DTI has opened new doors in studying various clinical pathologies in order to better understand and treat them.

2.4 Limitations of DTI

Although DTI has had a profound influence in the medical field, its potential is undermined by its inability to resolve the fine neural fibers as they branch out of the fiber bundles and terminate in the grey matter of the brain tissue. The resolution of DTI is currently, limited to 1 mm $\times$ 1 mm $\times$ 1 mm - isotropic, while the typical thickness of a neural fiber is 10 μm - 100 μm. Each voxel contains numerous fibers, not necessarily aligned in the same directions. DTI only calculates one fiber orientation per voxel. The method therefore, is unable to resolve multiple fiber orientations. Higher resolution, on the other hand, demands stronger and faster magnetic and gradient field strengths, which is not always possible, especially in a clinical setting.

DTI signal is much stronger in tissue regions where the white matter fibers are mostly unidirectional. In the presence of multiple fiber orientations, often referred to as intravoxel orientation heterogeneity (IVOH) , the degree of anisotropy is undermined and an averaged direction of diffusion (and hence fiber) is estimated which is often inaccurate.

The large voxel size also enhances the effect of partial volume. Partial volume effect is the presence of two tissue types in a voxel that cannot be distinguished from each other. Since diffusion in the GM is highly isotropic, presence of GM and WM both, in a voxel, further affects the anisotropy calculations.

Another problem associated with DTI is that it cannot distinguish whether the fibers cross each other or are two different pathways touching each other. As shown in Figure 7, the fibers may be crossing or just touching each other. DTI cannot detect the difference between the two cases and the outcome depends on the ROI selected for tracking.

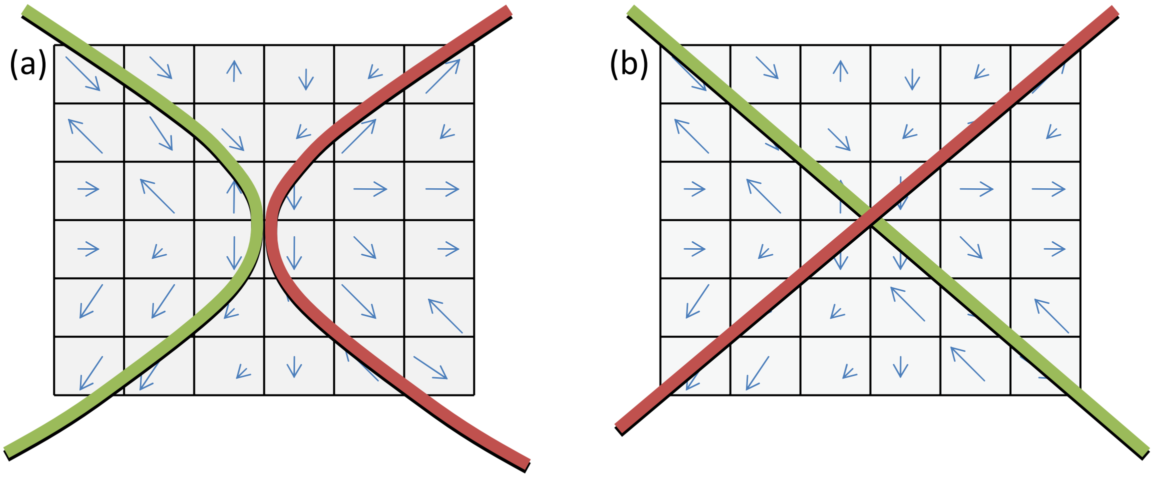

Figure 7: Limitation of DTI: (a) Crossing and (b) Kissing Fibers. The tensor estimation for both the cases is identical and fiber tracking algorithms cannot differentiate between the two.

Unlike histological tracing methods, DTI is unable to detect whether the fibers are afferent fibers or efferent fibers and hence smaller neural pathways that emanate midway between a larger, more prominent fiber bundle and run along the larger pathway, cannot be separated. For example, the tecto-geniculate pathway is a small neural pathway from the Dorsal Lateral Geniculate Nucleus (LGN) to the Superior Colliculus (SC). It runs alongside the optic tract from the optic chiasm to the SC via the LGN. Separation of these two tracts is not possible with the current DTI methods.

2.4.1 Recent Advances

There is significant promise in the use of DTI for studying fiber degeneration, regeneration and assessing neural pathways in the presence of tumors, especially for treating and studying individual difference across a population. However, the above limitations have proven as deterrents to the potential of this method. Recent studies have focused on using the complete tensor information i.e., $\epsilon_1, \epsilon_2, \epsilon_3$ obtained from D instead of just ϵ_1 to predict the presence of multiple fiber orientations [70]. The advanced fast marching technique [70] has greatly improved the performance of DTI tractography by detecting a profuse network of nerve fiber branches in the callosal region.

2.4.2 Alternative Techniques

Diffusion imaging has the advantage of being the only non-invasive technique that is used for mapping neural connectivity. Prior to the discovery of DTI and Positron Emission Tomography (PET) tracers, histology was the only window to study how different areas of the brain were connected. Due to the drawbacks of DTI outlined above, histology still remains the most popular technique for high resolution, region-specific study of neural connectivity. In DTI, diffusion process in the tissue is modeled as a Gaussian distribution which precludes the accurate determination of the diffusion profile in the presence of IVOH. Other diffusion imaging techniques that attempt to alleviate some of the limitations of DTI, such as High Angular Resolution Diffusion Imaging (HARDI) [77], Q-ball Imaging [76, 78] and Generalized Diffusion Tensor Imaging (GDTI) [40] have emerged.

- HARDI: HARDI samples the diffusion in the tissue along many more directions as compared with DTI. IVOH are identified in DTI by their oblate diffusion tensors ($\lambda_1 \approx \lambda_2$). In HARDI, the resultant diffusion is considered as a sum of the diffusion in individual compartments, each representing a unique fiber orientation. The individual diffusion tensors D_j and the fraction of diffusion, f_j, due to each diffusion tensor is computed by employing the mixture model decomposition to minimize the error function

  $$\chi = \sum_{k=1}^{n} \left(\sum_{j=1}^{m} Cp_{jk} - C_k \right)^2 \tag{19}$$

  where Cp_{jk} is the diffusion signal predicted by the model for the k_{th} diffusion gradient and the j_{th} fraction and C_k is the actual measure signal. The outcome of HARDI is shown in Figure 8.

- Q-ball Imaging: Unlike DTI, Q-ball imaging [76] does not assume any model for the diffusion process [57]. The Q-ball reconstruction is based on the interpolation of a spherical radial basis function and the Funk-Radon Transform. The orientation distribution function (ODF) is expressed in terms of the Funk Radon Transform, the diffusion probability density function and the zeroth-order Bessel Function. Visualization of the ODF reveals the presence of multiple fiber orientations and hence, offers the biggest advantage over tensor-based methods.

- Generalized Diffusion Tensor Imaging (GDTI): Generalized diffusion tensor imaging uses higher-order tensor statistics to obtain the diffusion profile in every

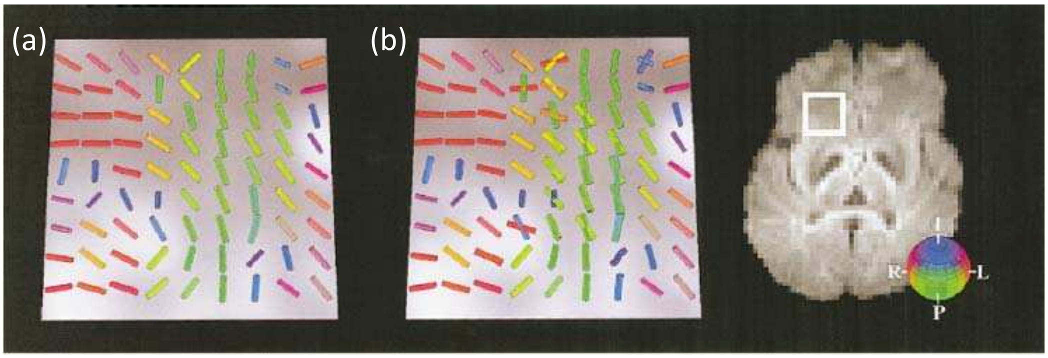

Figure 8: Comparison of the Principal Eigen Vector Fields from the (a) Single-tensor and (b) Two-tensor fits to Diffusion Signal from the Forceps Minor. The ROI is shown on the right. The vectors are oriented in the direction of the major eigenvector of the diffusion tensor within each voxel and are color-coded according to the RGB sphere shown at right, with red indicating mediolateral, green, anteroposterior, and blue, superoinferior. (b): The multitensor decomposition shows the intersections of the lateral and callosal striations with the anterior extension of the anterior limb of the internal capsule; and the divergence of fibers to the superior (bright green), middle (drab green), and inferior (red) frontal gyri. Note also the intersection between the anterolateral-directed fibers from the external capsule (bright green), and the superoinferior directed fibers from the uncinate fascicle (blue). Adapted from [77]

voxel [40]. The Probability Distribution Function (PDF) due to the diffusion of spins is reconstructed [39] using the higher order tensors followed by the estimation of a skewness map. The skewness map determines the extent of diffusion in different directions, enabling the estimation of fiber orientation.

Although the methods mentioned above have been successful in determining the presence of fiber crossings, the techniques require high-performance gradients and computationally intensive tensor calculations. Clinical application of techniques such as HARDI and Q-ball imaging is greatly restricted by these stringent requirements. On the other hand, DTI does not require such strong gradients or complex computations. Improvements in diffusion tensor imaging methods will provide a simple yet efficient way to accomplish accurate fiber tractography.

CHAPTER III

DIFFUSION TENSOR IMAGING AT LONG DIFFUSION TIME

Diffusion tensor imaging measures the net displacement of spins in a sample, due to random thermal motion, using a pair of diffusion gradients. These measurements are made over a preset duration called the diffusion time, t_{diff}. When the diffusion time is less, diffusion is dominated by perfusion effects of water molecules moving in and out of the cell. On the other hand, at higher t_{diff}, the diffusion is no longer sensitive to water perfusion. Diffusion of water molecules for $t_{diff} = 20$ ms is sufficient to probe the intra-cellular barriers that include large protein molecules and sub-cell organelles. Typically the diffusion time in DTI experiments is about 50 ms. The ADC decreases very rapidly over the first 20 ms [15] and drops more slowly until it reaches an asymptotic value. Clark *et al.* showed in a study that FA and ADC were unaffected during diffusion times in the range of 8 ms - 80 ms, as did Le Bihan *et al.*[36]. These measurements were made in core white matter regions such as the genu of the corpus callosum. White matter fiber bundles in this region are very tightly packed and highly oriented in one direction. Diffusion in such white matter structures is highly restricted. In addition, the b value was much smaller (700 s/mm^2) and the value of δ was changed to achieve the different diffusion times. Further, no data was provided for the second and third eigen vectors of D. Another study [26] showed that the ADC value was indeed dependent on time (40 ms - 800 ms), but the study involved an increase in the b value with increase in t_{diff}. Studies [50] have shown that an increased b value increases the sensitivity of DTI towards diffusion anisotropy.

As the nerve fibers project to the cortical surface, they fan out, causing a decrease in the degree of tissue organization. Applying Einstein's equation, $r = \sqrt{6Dt_{diff}}$, a t_{diff} of 20 ms is sufficient to explore distances of about 10μm, which is of the order of a typical brain cell. However, at much higher diffusion times, the diffusing water molecules are more likely to fine-tune the sampling of the diffusion space in and between the axonal fibers and the fiber bundles. Fractional anisotropy at longer t_{diff} has been reported to be more sensitive to changes in myelin-deficient mice [54]. DTI tractography at long diffusion times has not yet been reported in the literature. The present dissertation is based on the hypothesis that ***the use of longer diffusion time in DTI will increase the sensitivity of the technique to diffusion anisotropy and therefore, enhance our capability to resolve and track smaller nerve fibers.*** Figure 9 depicts the increase in diffusion anisotropy due to the use of long diffusion time in the brain tissue and its impact on tractography.

The intra-cellular and extra-cellular diffusion processes in the brain tissue are very complex and depend on a number of factors [52] such as the density of the intra-cellular organelles, macro-molecules, viscosity of extra-cellular fluid, tortuosity in the Extra-Cellular Matrix (ECM) [58], permeability and active transport through the channels, to name a few. It is very difficult to explain the contribution of each of the above factors to the diffusion measured by DTI. Further, a coherent explanation of the temporal dependence of these factors on ADC and FA is not yet available. Nevertheless, an attempt is made in this chapter to explain the rationale of the proposed hypothesis.

Figure 10 [1] describes different scenarios that can be encountered by the diffusing water molecules and the effect of the use of long diffusion time in improving the accuracy of tensor estimation using DTI.

This chapter describes the sequence design and modifications executed to allow DTI studies at long diffusion time. The pulse sequence and the imaging protocol

---

[1] Volume Fraction is the volume occupied by one fiber bundle relative to the voxel size

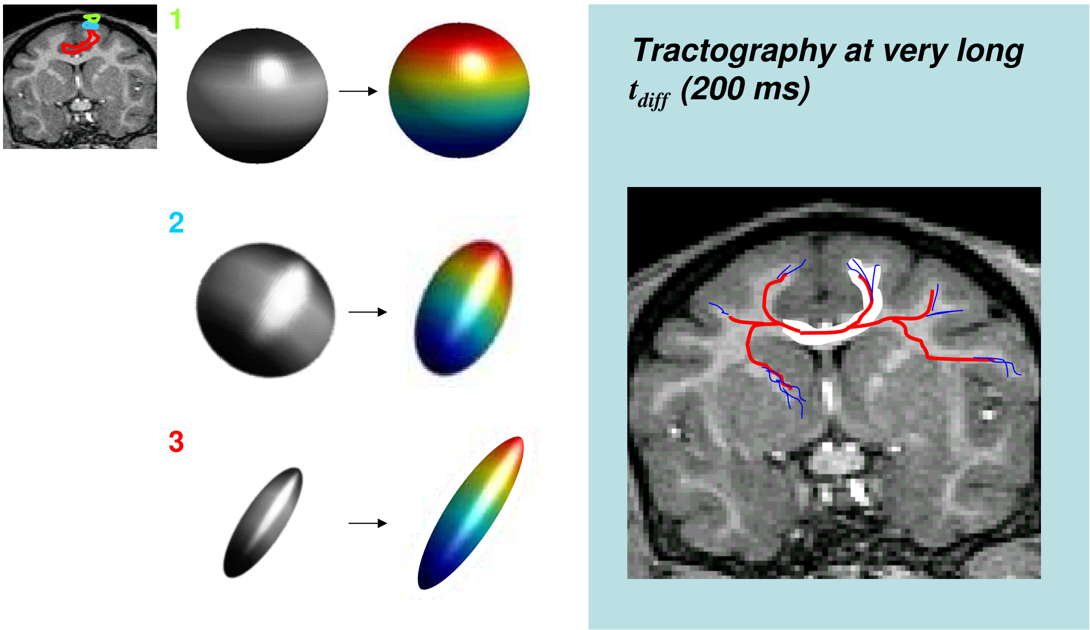

Figure 9: Pictorial Depiction of the Changes in the Diffusion Ellipsoid and Tractography Outcome with the Application of Long Diffusion Time: The inset shows three regions; 1 is core GM, 2 is a region of thinning WM fibers and GM interspersed in the same voxel and 3 represents core WM tissue. With the use of long diffusion time, it is anticipated that the diffusion ellipsoid in region 2 would become more oblong, providing a tensor with a higher magnitude that can be tracked using a DTI tractography algorithm. Region 1 (GM) is isotropic and hence there will not be any change in the diffusion even at long t_{diff}. In the core white matter tissue (region 3), the tensor magnitude will remain the same or increase slightly. Region 3 will provide a dominant fiber direction, independent of the diffusion time. Due to the increased sensitivity of DTI at long t_{diff} to the diffusion anisotropy, a dominant tensor orientation will be obtained in region 2, which is otherwise not possible at short t_{diff}. The fibers in red represent the fibers delineated with DTI at short t_{diff}. The blue fibers indicate the improvement that will be seen with the use of long t_{diff}

were tested on a phantom to verify its usability and to correct for any artifacts. The hypothesis was then tested using formalin-fixed brains. Once it was confirmed that the use of long diffusion time indeed improved nerve fiber tracking, the imaging sequence and protocol was further modified and translated to *in vivo* studies in rhesus macaques.

Non-human primates show considerable anatomical similarity to humans, in the neural tissue and hence serve as a good model to understand neural tissue structure

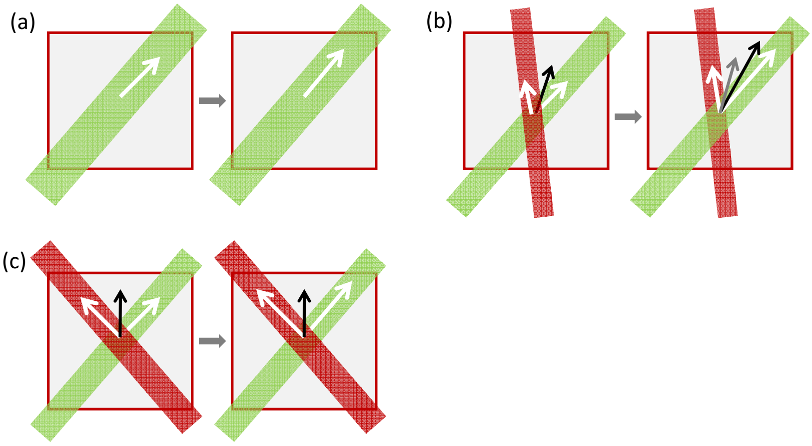

Figure 10: How Might Long t_{diff} Improve Tractography? The figure depicts different conditions the diffusing water molecules may be subject to. In each sub-figure, the voxel on the right represents the diffusion tensors that will be obtained at short t_{diff} and the voxel on the left depicts the speculated sampling that makes the calculated tensor orientation at long t_{diff}, more accurate. (a) Presence of one highly oriented fiber bundle (e.g., corpus callosum) The tensor orientation does not change. However, the tensor magnitude increases at long t_{diff}. (b) Presence of two fiber bundles with distinct volume fractions: A short t_{diff} is insufficient to calculate the accurate fiber direction. At long t_{diff}, the diffusion in the dominant fiber bundle is accentuated as more water molecules travel farther and have more hits. (c) This figure represents the condition in which the two fiber bundles as orthogonal to each other and have the same volume fraction. Under such a condition, the use of long diffusion time will not provide any extra information for DTI. (black arrow: resultant tensor, grey arrow: resultant tensor at short t_{diff})

and study evolutionary changes that may have occurred in the architectonical mapping of the brain [68, 47, 79]. One of the main concerns in non-human primate DTI is the selection of the appropriate resolution in accordance with the anatomy, the relative fiber sizes, required SNR and the available acquisition time. In tensor-based tractography, besides affecting the mean fiber density, resolution directly impacts the estimation of the apparent diffusion tensor and hence the orientation of the underlying nerve fiber [32]. A higher resolution reduces partial volume effects and facilitates a more accurate inference of the tensor, although at the expense of a longer scan time due to increased averaging in order to compensate for the SNR loss. Human DTI studies are usually conducted at a isotropic in-plane resolution of 1.2 mm - 3 mm.

However, a rhesus macaque brain is significantly smaller than the human brain and requires a much higher image resolution. The average volume of the human brain (male) is found to be around be about 1450 cc [47, 79]. Brain size in chimpanzees is roughly 400 cc [68] while the macaque brain is relatively much smaller at 103 cc [18]. To achieve the same resolution as human studies the ideal voxel size for DTI imaging in chimpanzees would be 1.5 times smaller along each dimension while for macaque studies, the voxel size would be smaller by a factor of 2.5 per side. Diffusion tensor imaging in rhesus macaques, however, is currently performed at a resolution of 1mm × 1 mm × 1mm. DTI scans with a resolution lower than 1 mm × 1 mm (in-plane), often use a much higher slice thickness to gain SNR. In this study, an attempt was made to use as high resolution as was possible on the 3T Siemens 3T Trio at least for the *ex vivo* scans.

3.1 Sequence Modification and Coil Setup

Conventionally, a spin echo sequence [73] or a twice-refocussed spin echo sequence [66], also known as the Double Spin Echo (DSE) sequence is used for DTI studies. However, it suffers a very high signal loss at higher values of t_{diff} due to a significant $T2$ decay. To overcome the high SNR loss, a Stimulated Echo Acquisition Mode (STEAM)-EPI [23, 46] sequence was used for DTI studies at long t_{diff}. The STEAM sequence utilizes three 90° pulses instead of one 90° and one or two 180° pulses in DSE. This facilitates increased diffusion times at much shorter TEs. On the flip side, only half the transverse magnetization is used for signal generation in STEAM, thereby halving the SNR. Further, the DSE sequence efficiently reduces the effect of eddy current distortions and susceptibility related artifacts. These artifacts are not corrected for in the STEAM sequence. However, the shorter TE at least partially compensates for the signal loss. Additionally, the crusher gradient strengths were increased to remove any residual echo. The pulse width and the slice select gradient was adjusted to allow high resolution DTI scans without increase in cross-term artifacts along the direction (Z) of slice selection.

For the *ex vivo* studies, the t_{diff} value was increased gradually and the increase in FA and the SNR of the images was evaluated. The FA increased gradually with increasing t_{diff}. However the SNR reduced significantly around $t_{diff} \approx 230$ ms. The longest usable diffusion time was determined by a limitation on the SNR. The imaging protocol is described in Table 2. The design was optimized for the highest resolution (0.54 mm × 0.54 mm in-plane) possible with the 3T Trio system for two values of t_{diff}; 48 ms and 192 ms. The two sequences will be referred to as STEAM48 and STEAM192 henceforth. The DSE sequence was also implemented to verify that the improvement was indeed due to the use of long diffusion time and that using the STEAM sequence did not affect DTI acquisition. The t_{diff} for the DSE sequence was 45 ms. The imaging parameters were almost the same except as mentioned in the table. The number of averages were adjusted to achieve similar SNR for all three acquisitions.

Table 2: *Ex Vivo* Study: Imaging Protocol

Imaging Parameter	**Value**
TR	1500 ms
TE	80 ms (STEAM), 104 ms (DSE)
b	0,1700 s/mm^2
TM	21 ms for t_{diff} = 48 ms, 169 ms for t_{diff}=192 ms
Number of Directions	30
Slice Thickness	2 mm
Number of Slices	3
Field of View (FOV)	70 mm × 70 mm
Matrix Size	128 × 128
Number of EPI Shots	16
Bandwidth (BW)	448 Hz/pixel (STEAM), 472 Hz/pixel (DSE)
Averages	48 (DSE), 37 (STEAM48), 70 (STEAM192)
SNR	29.78 (DSE), 27.01 (STEAM48), 26.80 (STEAM192)

The *in vivo* studies required a further modification in the STEAM sequence in order to fit the total acquisition time within a time window of about 3.5 hours. The

STEAM sequence was further modified to adjust the fill times that are inserted for accurate echo acquisition. The fill times added to t_{diff}, result in a higher TE and preclude a smaller value of t_{diff} from being achieved. This fill time is shown in Figure 11. In order to overcome this problem, the fill time was introduced before the execution of the diffusion gradients.

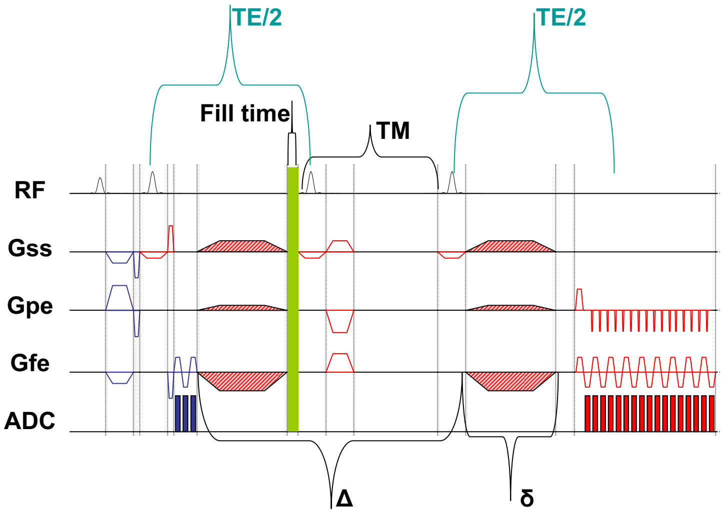

Figure 11: STEAM Sequence for *In Vivo* studies: The fill-time shown by the green band adds to the calculation of t_{diff} This fill time was shifted and added before the diffusion gradients were applied. Thus, a smaller t_{diff} could be achieved at the same TE. RF: Radio Frequency Pulse, Gss: Slice Selection Gradient, Gpe: Phase Encoding Gradient, Gfe: Frequency Encoding Gradients, ADC: Analog to Digital Converter

High resolution, *in vivo* scans could not be acquired due to the gradient limitations and the necessity to obtain a high SNR in a relatively smaller total acquisition time as compared to the *ex vivo* studies. Each study included at least two sets of DTI experiments, one at short t_{diff} and one at long t_{diff}. The number of EPI shots and the resolution were altered to reduce scan time. The two diffusion times used for *in vivo* studies were 50 ms and 200 ms The two sequences will be known as STEAM50 and STEAM200 henceforth. t_{diff} for DSE was 47 ms. The imaging parameters are shown in Table 3.

The value of TE in the STEAM sequences at long diffusion times is purposely maintained at the same value that was used in the STEAM sequence at short diffusion

Table 3: *In Vivo* Study: Imaging Protocol

Imaging Parameter	Value
TR	5000 ms
TE	60 ms (STEAM), 91 ms (DSE)
b	0,1200 s/mm^2
TM	34 ms for $t_{diff} = 50$ ms, 184 ms for t_{diff}=200 ms
Number of Directions	60
Slice Thickness	1 mm
Number of Slices	5
Field of View (FOV)	64 mm × 64 mm
Matrix Size	64 × 64
Number of EPI Shots	4
Bandwidth (BW)	1042 Hz/pixel (STEAM), 1056 Hz/pixel (DSE)
Averages	3 (DSE), 3 (STEAM50), 6 (STEAM200)
SNR	28.45 (DSE), 24.58 (STEAM50), 22.87 (STEAM200)

times. The same b value of 1700 s/mm^2 is maintained at long t_{diff} by using diffusion gradients with reduced magnitudes. In principle, TE can be reduced by utilizing a higher strength of diffusion gradients to maintain the b value. This study compared the DTI data acquired at two different diffusion times. If the TE is changed, then the $T2$ weighting of the GM and WM tissue changes across the two experiments in addition to the diffusion time. For e.g., as shown for the *ex vivo* studies in Figure 12, the three eigen values and ADC was measured at a t_{diff} of 192 ms for a TE of 65 and 80 ms. The ADC, λ_1, λ_2 and λ_3 were significantly different at the two TEs ($p < 0.05$). TE was therefore, unchanged to avoid any bias in the comparison due to differential $T2$ weighting in the brain tissue.

3.1.1 Cross-term Correction

Diffusion measurements in DTI are a consequence of the application of a pair of diffusion gradients alone. In practice the diffusion measurement can also be affected by the interaction of the diffusion gradients with the imaging gradients and the interaction of different imaging gradients amongst themselves, resulting in an incorrect measurement of ADC. This effect is called as the cross-term effect and must be kept

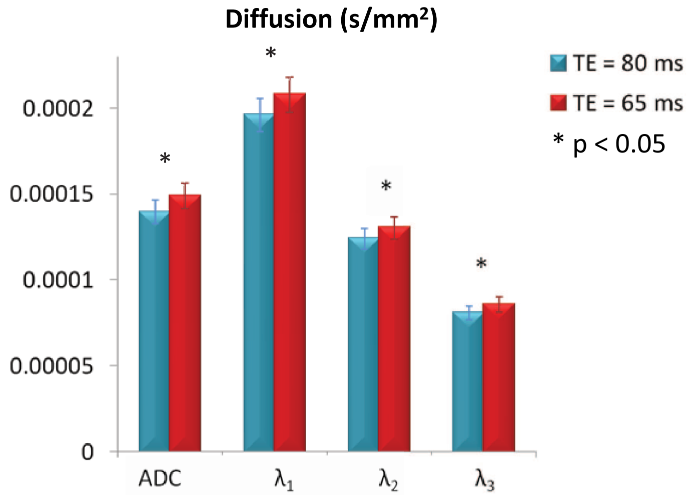

Figure 12: Calculation of ADC, λ_1, λ_2 and λ_3 for $t_{diff} = 192$ ms at TE $= 80$ ms (blue) and TE $= 65$ ms (red). The bar graph represents the mean value ± standard deviation over all the slices acquired in the experiment. ROIs (about 20 voxels each) were selected in the corpus callosum and the internal capsule.

at a minimum. For this purpose, the b matrix (Eqn. 11) can be computed analytically [45] to determine the contribution of the different gradient interactions towards the diffusion measurement. These calculations are much more complex for DSE and the STEAM sequence. An alternative approach that was used in the present research, involves geometric averaging [55, 22] to reduce cross-term interaction . For every DW image acquired at a diffusion directon, another DW image is acquired in the same diffusion direction but with the gradient directions inverted. For e.g., if the DW image was once acquired along (X, Y, Z) direction, another image is acquired at (-X, -Y, -Z) direction. The b value can be split into three additive components:

b_d: Due to the effect of diffusion gradients,

b_{ct}: Due to the interaction of imaging and diffusion gradients and

b_{img}: Due to the interaction of the imaging gradients.

Therefore, $b = b_d + b_{ct} + b_{img}$. For an image acquired with the inverted gradients, the b value becomes $b_d - b_{ct} + b_{img}$. When the two images are multiplied together on a pixel by pixel basis, b_{ct} term cancels out (20). The cross-terms due to the imaging gradients is not canceled but the effect of these gradients is usually minimal.

$$S = \sqrt{S^{+}S^{-}} = \sqrt{S_0 e^{-b^{+}D} S_0 e^{-b^{-}D}} = S_0 \sqrt{e^{(b_d + b_{ct} + b_{img})D} e^{(b_d - b_{ct} + b_{img})D}}$$

$$= S_0 e^{(b_d + b_{img})D} \approx S_0 e^{b_d D} \tag{20}$$

The main disadvantage of this method is that the acquisition time is doubled. The SNR obtained after geometric averaging is always less than the SNR obtained with the arithmetic mean of two images. This loss can be compensated by increasing the number of averages at the cost of increased total acquisition time.

3.1.2 Coil Setup

To increase the SNR of each image acquisition, a custom-built surface coil (courtesy, Athinoula A. Martinos Center of Biomedical Imaging, Massachusetts General Hospital, MA 02129) was used. The SNR increased by approximately 30% with the use of this coil as compared with a standard volume coil used for primate imaging. The coil interface with the Siemens 3T Trio machine, used for this study is shown in Fig.(13). Additionally, a testing rig was built for testing the pre-amplifier used in the receiver circuit. (Details of the circuit are not shown due to confidentiality agreement with Siemens)

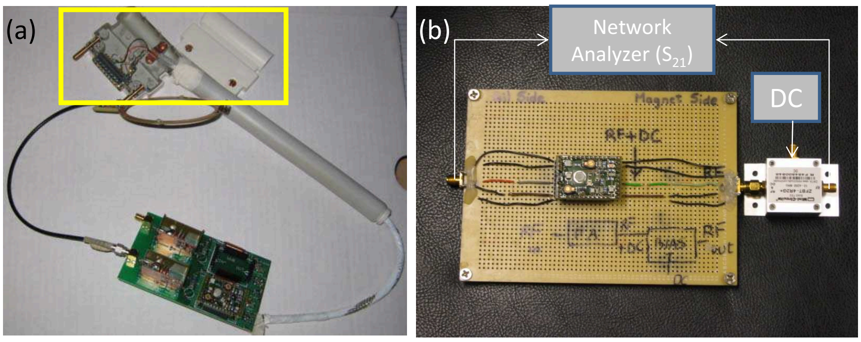

Figure 13: Coil Design and Interface for the Custom-built Surface Coil used in the Present Work.

3.1.3 Phantom Selection and Setup

In order to test the imaging sequence and optimize the protocol, a spherical ($\phi = 45$ mm) isotropic phantom was filled with 0.5 M Mannitol dissolved in Dimethyl Sulfoxide (DMSO). The ADC of Mannitol [16] in water is 0.90×10^{-3} mm^2/s. Although the ADC of Mannitol in DMSO is not known, it was expected that the ADC would be closer to that of water in the brain tissue (0.76×10^{-3} mm^2/s) [35] as against the ADC of water in an isotropic phantom (2×10^{-3} mm^2/s). The similarity in ADC would facilitate the choice of imaging parameters befitting the *ex vivo* and *in vivo* studies.

For cross-term correction, the average ADC value for the phantom was used as the reference (0.39×10^{-3} mm^2/s). Early testing revealed that there were significant cross-terms along the slice selection (SS) and the read-out (RO) direction. Ideally, the ADC measured along any axis should be identical for a isotropic phantom. However, it was observed that, as the t_{diff} is increased, the ADC measured along the three axes varied more as shown in Figure 14.

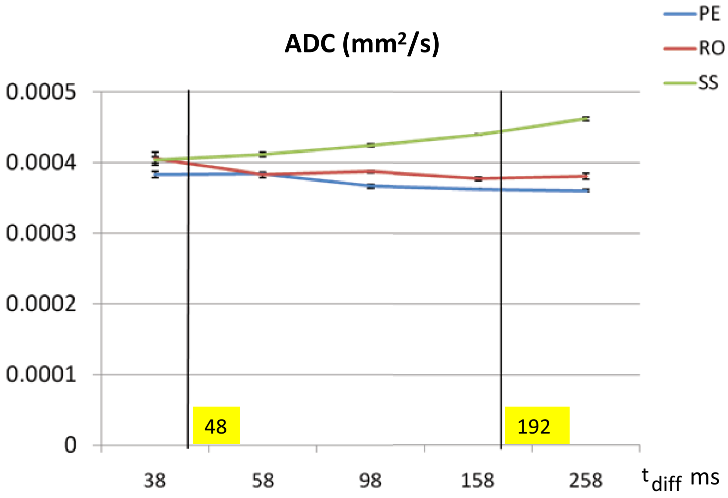

Figure 14: Variation of ADC along the Three Axes (PE, RO and SS) with t_{diff}. PE: Phase Encoding (X Axis), RO: Read Out (Y Axis), SS: Slice Selection (Z Axis) It can be seen that the effect of cross-terms worsens with increase in diffusion times. The difference in the ADC values calculated along the three axes for the two diffusion times (48 ms and 192 ms) that were used for *ex vivo* studies are marked by the vertical black lines.

For the *ex vivo* studies, the maximum difference in the ADC in an isotropic phantom was about $8.1 \pm 1.1\%$ at $t_{diff}=$ 48ms and approximately $14.3 \pm 1.4\%$ at $t_{diff}=$ 192ms. After correction, these differences reduced to $3.3 \pm 1.7\%$ at $t_{diff}=$ 48 ms and $5.4 \pm 1.7\%$ at $t_{diff}=$ 192 ms. The plots for geometric averaging done across the three axes for $t_{diff}=$ 48 ms and 192 ms are shown here in Figure 15(a). Similarly, geometric averaging was performed for the *in vivo* studies (Fig. 15(b)). The maximum variation in ADC reduced from $10.4 \pm 2.3\%$ to $3.1 \pm 0.5\%$ at $t_{diff}=$ 50 ms and from $13.4 \pm 3.1\%$ to $4.7 \pm 1.0\%$ at $t_{diff}=$ 200 ms. For the DSE sequence, the cross-terms were much lower with a maximum variation in the ADC value was $3.8 \pm 1.0\%$ for the *ex vivo* studies and $5.0 \pm 1.2\%$ for the *in vivo* experiments. Hence, the correction was not implemented for DSE.

Unfortunately, geometric averaging does not remove the effect of interactions of the imaging gradients. This results in the application of a non-uniform b-value along the three axes and can adversely affect the accurate estimation of ADC. Ideally, the ADC of an isotropic phantom calculated by any sequence should be identical. To study this effect, an experiment was performed to measure the ADC of the mannitol phantom at different b-values at the different diffusion times used in this study. Geometric averaging was performed on the data. As seen in Figure 16, the slope of $ln(S/S_0)$ is the same for the shorter diffusion times in both *ex vivo* and *in vivo* studies. However, they do not coincide with one another, indicating that the ADC calculated by the two methods would be different. The difference is proportional to the offset between the 2 slopes. For the longer diffusion times, in both *ex vivo* and *in vivo* studies, the slope and the offset of the $ln(S/S_0)$ lines is different. For the *ex vivo* imaging parameters, the ADC calculated with DSE can be similar to or slightly higher than the ADC calculated with STEAM at long t_{diff}. The imaging protocol used in *in vivo* studies predicts that the ADC calculated with STEAM at long t_{diff} $<$ DSE $<$ STEAM at short t_{diff}. Hence these values cannot be used for establishing the accurate dependence

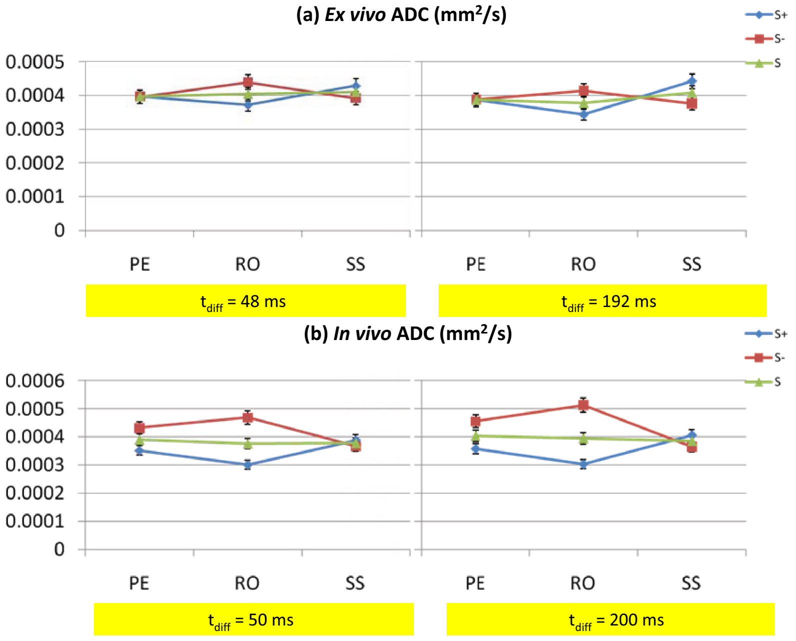

Figure 15: Geometric Averaging: (a)*Ex vivo* studies: The plots show the variation in ADC along the phase encoding (PE), read-out (RO) and slice selection (SS) directions for t_{diff}= 48 ms (left) and t_{diff}= 192 ms (right). Similar results are shown for the *in vivo* studies (b) for t_{diff}= 50 ms (left) and t_{diff}= 200 ms (right). The red and blue curves indicate the ADC values obtained with opposite gradient directions and the green curve represents the ADC values obtained after geometric averaging. Geometric averaging is very effective at minimizing the effects of cross-term interactions. (S^+: DWI image obtained with one set of diffusion gradients, S^-: DWI image with the same diffusion directions as S^+ but with opposite magnitude of the diffusion gradients, S: corrected image)

of ADC on diffusion time. However, the parallel and perpendicular diffusivities can be used to determine the changes in D with increase in diffusion time. Further, the ratio of parallel diffusivity to perpendicular diffusivity will corroborate the increase in anisotropy, observed at long diffusion time.

3.2 *Ex vivo fixed brain experiments*

Study of *ex vivo* nerve tissues has provided significant data on the dependency of ADC on diffusion time [11, 62]. In particular, fixed tissue samples serve as good protoypes for studying anatomy [72, 14, 33]. For *ex vivo* studies, imaging protocols can be optimized for superior image quality in terms on high SNR and resolution. *Ex vivo*

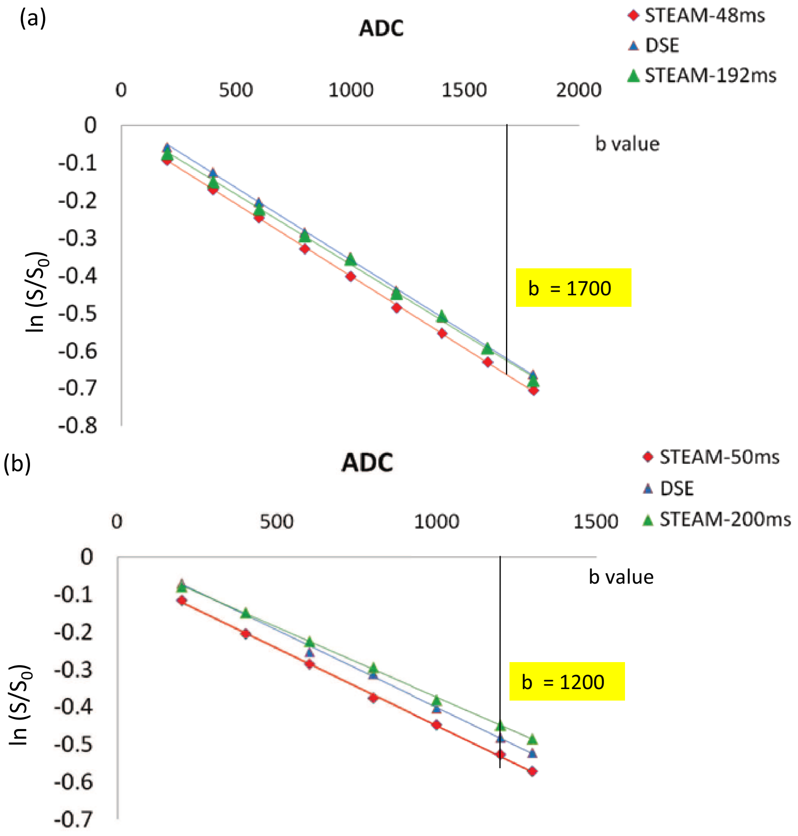

Figure 16: Effect of b value on ADC: $ln(S/S_0)$ is plotted against b values. The trend for the three sequences can be seen. For the *ex vivo* study, the ADC calculated using STEAM48 is higher than that calculated by STEAM192 and DSE. Due to the residual cross terms, the ADC calculated by STEAM192 and DSE does not appear significantly different. However, for the *in vivo* protocol, the ADC calculated by STEAM200 is the least, followed by DSE and STEAM50. Ideally, the ADC with STEAM at short t_{diff} and DSE at short t_{diff} must be identical.

studies also have an advantage due to the absence of any physiological noise. Studies [72] have shown that DTI parameters are not significantly affected by formalin-fixation of the nervous tissue. Although, the SNR in formalin-fixed mice brains is lower, the relative SNR [1] in different white matter tracts was similar to that in *in vivo* studies. RA values, tensor orientations, and longitudinal and radial diffusivities normalized by D were similar to those calculated *in vivo* [72]. However, the ADC values were significantly reduced (by approximately 0.5 times the ADC calculated *in vivo*). DTI

---

[1] Relative SNR refers to the difference in the SNRs of different regions in the brain

studies in fixed primate brains further showed that DTI parameters are affected by the time interval between death of the organism and completion of the fixation process. This duration is known as Post Mortem Interval (PMI) [13]. As PMI increases, the increased tissue degeneration causes an increase in the ADC and decrease in the FA. Thus, although formalin-fixed brains are excellent choices for neurological and neuro-pathological studies using DTI, the fixation process is critical to obtain results similar to that of *in vivo* studies. In any case, the relative difference in the tissue composition and orientation across different neural pathways is maintained even after fixation. Hence, formalin-fixed brains serve as excellent models to study the brain structure.

For the *ex vivo* fixed brain studies, the tissue was perfused-fixed in 10% formalin and 4% formalin. Initial experiments showed that the SNR obtained with 10% formalin-fixation was low. In this study, WM $T2$ was 42 ms in 4% formalin and 40 ms in 10% formalin. GM $T2$ was 47 ms in 4% formalin and 42 ms in 10% formalin. It is conjectured that the similarity between GM and WM $T2$ in the 10% formalin could be due to the reduction in the mobility of water upon fixation. Pfeufferbaum *et al.* [64] suggest in their study that the difference between the mobility of water in the GM and WM decreases due to fixation and also decreases over time. Contrary to the notion that GM is isotropic, early experiments showed that the FA in the GM for 10% formalin-fixed brains increased significantly with increase in t_{diff}.

A possible reason for the increased FA in the GM for the 10% formalin-fixed brains could be the reduced SNR obtained with 10% formalin fixation. The $T2$ in GM was lower by 5 ms in the 10% formalin-fixed sample as compared in the 4% formalin-fixed sample. This decrease in T2 itself by 5 ms causes a drop in the signal intensity of 20% in the GM and could cause an erroneous measurement of DTI parameters at lower SNR values.

Since the FA of the GM remained independent of t_{diff} in the 4% formalin-fixed samples, and since the SNR was about 29% higher in 4% formalin fixed brains, they were used to confirm the hypothesis of this study. Four 4% formalin-fixed tissue samples were used. Eight experiments were performed on these brain samples. The same protocol was used for the validation of the tractography results. In order to minimize the susceptibility artifacts at the tissue-air surface, the tissue sample was washed thoroughly and immersed in water. However, the surrounding water gave rise to a strong signal of the water from the edges of the phantom and caused Gibbs Ringing. This can be seen in the form of a checker board pattern in the tissue sample. To remove the ringing artifact, 0.018 mg/ml of Magnetic Iron-Oxide Nano-compounds (MIONs) was added to the water to annul the signal of water. Figure 17 shows that the addition of MIONs efficiently eliminates Gibbs Ringing and the checker board pattern is completely removed. The MIONs were large enough to remain outside the brain tissue. This was verified by acquiring $T1$ and $T2$ weighted images of the sample over 1 week.

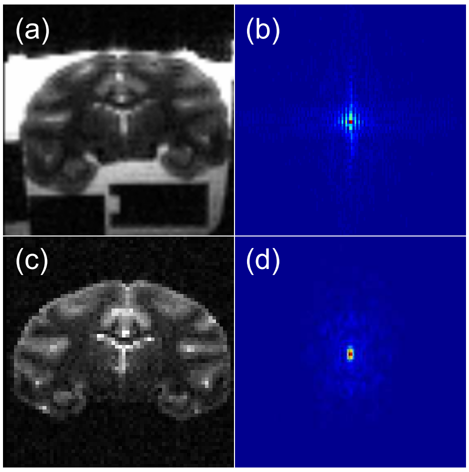

Figure 17: Gibbs Ringing Artifact : (a)Fixed brain sample immersed in water. The ringing artifact arising from the edges of the container can be clearly seen in the image and the kspace data (b). (c) and (d) show the image and the corresponding kspace data after the addition of MIONs.

In all experiments, $T1$-weighted anatomical data was acquired to evaluate slice positioning and for intensity based segmentation of WM and GM. $T1$ weighted images were acquired using a Fast Low-Angle Shot(FLASH) sequence. The imaging parameters were: $TR = 200$ ms, $TE = 7.7$ ms, FOV = 70 mm × 70 mm, matrix size = 128 × 128, slice thickness = 2 mm, flip angle = 25° and the number of averages = 2.

3.3 In vivo fixed brain experiments

For the *in vivo* studies, the animals were first anesthetized with Telazol (3-5 mg/kg). The ears were coated with EMLA Cream and the eyes with PuraLube. Lactate ringer solution was delivered via an intra-venous line to the animal during the scan. The animal was placed in a cradle and the head was immobilized using a mouth-piece and ear-bars. The animal was anesthetized using 1 - 1.5% isofluorane during the experiments. The experiment involved obtaining $T1$-weighted anatomical scans followed by 2 sets of DTI scans, one at short t_{diff} and one at long t_{diff}. The animals are recovered completely before returning them to their cages. Five rhesus monkeys were used in each set of study. Six experiments were conducted on these animals using the procedure described.

The *in vivo* studies have the advantage of longer relaxation parameters ($T1$ and $T2$) thereby providing a higher SNR. Along with the modifications to the STEAM sequence described earlier, the total acquisition time for these scans was drastically reduced. To minimize physiological noise, the experiments could have been converted to a single-shot EPI study. However, the SNR drops significantly with single-shot EPI, especially for the STEAM sequence. The TR was adjusted to a multiple of the respiration rate to reduce the effect of physiological noise and 4-shot EPI data was acquired. After image acquisition, images that contained a significant ghosting artifact were removed. The quality of the images was determined by visual inspection.

In the *in vivo* experiments, $T1$-weighted anatomical data was acquired to evaluate slice positioning and to perform intensity based segmentation of WM and GM. $T1$ weighted images were acquired using a FLASH sequence. The imaging parameters were: TR = 3500 ms, TE = 135 ms, FOV = 100 mm × 100 mm, matrix size = 256 × 256, slice thickness = 2 mm, flip angle = 25° and the number of averages = 2.

CHAPTER IV

EX VIVO AND *IN VIVO* STUDIES OF DTI AT LONG DIFFUSION TIME IN RHESUS MACAQUES

4.1 Data Analysis

Various parameters such as FA, ADC and DE were calculated for the three acquisition schemes: DSE, STEAM at short t_{diff} and STEAM at long t_{diff} to evaluate the effect of employing long diffusion time for DTI tractography. Then fiber connectivity was compared using fast marching and line propagation. The details of the analysis and the comparison follow next.

4.1.1 Diffusion Parameters

Fractional anisotropy and ADC were measured in the white and grey matter in all the acquired images. White and grey matter were segmented using $T1$ weighted images. A student t-test was performed on the FA and ADC data to verify if the difference was statistically significant [1]. Based on the hypothesis of this study, the use of long t_{diff} should provide tensors with a higher magnitude and consequently should have a higher FA in the WM voxels.

4.1.2 Geometric Diffusion

The CL, CP, and CS measures of diffusion provide an insight into the shape of the diffusion profile, giving an idea of the underlying tissue arrangement. The three-phase (3P) plots is a convenient and useful approach to study how the shape of the diffusion profile changes with the use of a longer diffusion time. These plots are obtained as

---

[1] A Student t-test is a simple satistical method to test a hypothesis on the basis of the mean of two sample distributions.

follows:

$$x = \frac{1 - CP + CL}{\sqrt{3}} \tag{21}$$

$$y = 1 - CP - CL \tag{22}$$

Diffusion anisotropy is then classified on a triangle with isotropic diffusion represented by CS at the apex of the triangle, CL at the left vertex and CP at the right vertex. Figure 18 represents the three phase plots . Any diffusion in the tissue can now be represented in this triangle. If the diffusion profile shifts towards CL or CP, then it can be assumed that the application of long t_{diff} indeed, increased the sensitivity of the technique to diffusion anisotropy. A deflection towards CL would reflect an increase in the linear diffusion and would indicate tensors with larger magnitude that can be conveniently used for fiber tracking. A deflection towards CP would represent an increase in the detection of fiber crossings. Such voxels may be useful in the advanced fast marching method to detect fiber branching [70].

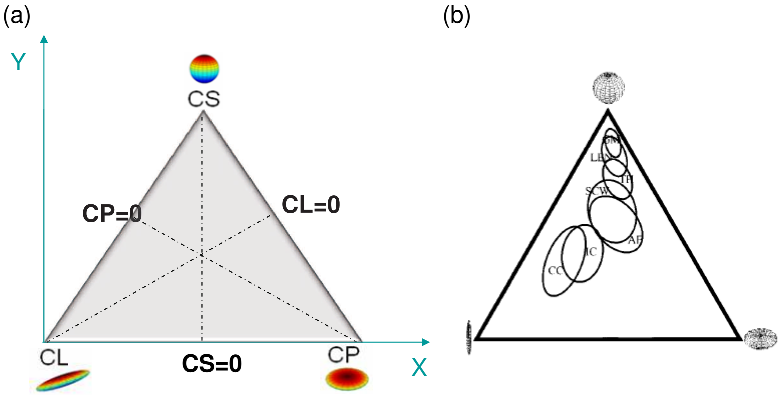

Figure 18: Three-Phase Plots: (a) The triangle representing geometric diffusion obtained using Equations 21 and 22. (b) Isocontours of one standard deviation from the mean location in 3P space are plotted. The distributions are highly overlapping in three groups of tissues: 1) corpus callosum (CC) and internal capsule (IC), 2) arcuate fasciculus (AF) and sub-cortical white matter (SCW), and 3) gray matter (GM), lentiform nucleus (LEN) and thalamus (TH).(b), reproduced from [2]

The means of the scatter plots and the distribution of the values of x and y

(Equations 21 and 22) were obtained for the selected ROI, for each acquisition were calculated. A Student-t test can ony be used for a sample dstribution that is normal or if the sample size is large enough. Lilliefors test was used to test the goodness of fit of these distribution to a normal distribution. It was observed that the distributions were not normal and a Kolmogorov-Smirnov test was used instead to determine whether the distributions obtained for the different acquisition schemes were significantly different.

4.1.3 Directional Entropy

Traditionally, directional entropy, DE, is calculated over the whole brain volume. Since there is a lot of variance in the directions of the principal eigen vector across all the voxels, the whole brain DE is not very useful for analysis. DE is therefore, calculated for every voxel using a $5 \times 5 \times 5$ voxel-neighborhood [56], and then averaged over the acquired volume. However, in this study, DE was calculated over a region that encompasses core white matter tissue and white and grey matter interfaces. It is believed that DTI at long t_{diff} not only provides a higher FA but also emphasizes the dominant fiber bundle in a voxel with IVOH. In that case, the orientation of the tensor will be more coherent with the tensor orientations in the adjacent voxels. DE then, should reflect such an increased coherence by a decrease in its value. For calculations of DE in this study, the sphere was triangulated into 196 faces. DE was measured along the callosal projections and the cortico-pontine and cortico-bulbar tracts.

4.1.4 Fast Marching Method

Fast marching method is used for determining the probabilistic connectivity map or a front that depicts the likelihood of an arbitrary point being connected to a chosen seed point. There are different rate equations to obtain the connectivity front. The rate equation used for this study is given by Equation (23) [59]. The rate of evolution, f (shown in Figure 19) of the surface/front from position r to r' in the brain volume is given by

$$f = \frac{1}{(1 - min(|\epsilon_1(r) \cdot n(r)|, |\epsilon_1(r) \cdot \epsilon(r')|)} \tag{23}$$

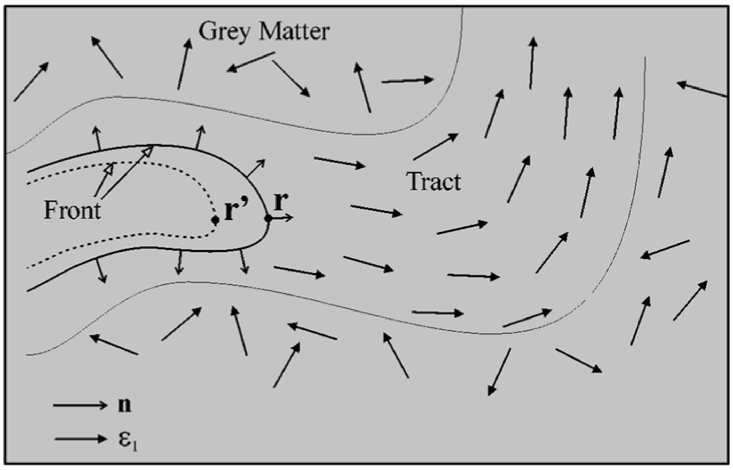

Figure 19: Fast Marching Technique: The principal eigen vector of diffusion, ϵ_1, is arranged in a directionally coherent manner in tracts, while in grey matter this coherence is largely lacking. The relation between the front f, $\epsilon_1(r')$, $\epsilon_1(r)$ and $n(r)$ is shown. Reproduced from [59].

where $\epsilon_1(r)$ is the principal eigen vector at position r

$\epsilon_1(r')$ is the principal eigen vector at position r'

$n(r)$ is the normal to the front at r and describes the direction of evolution of the front. The front propagation was terminated when the connectivity is 50% of the maximum connectivity in *ex vivo* studies and was 35% of the maximum connectivity for the *in vivo* studies. The threshold at which the front moved outside the brain tissue was used as the cut-off threshold.

4.1.5 Line Propagation

For fiber tractography, DTI Studio v2.4 [28] and dTV [44] were used. Seeds were placed in the corpus callosum, cortico-pontine, cortico-bulbar and cortico-striatal fiber bundles. Although these are prominent fiber tracts in the macaque brain, finer fiber branches of the callosal tract especially in the paracentral gyrus and the precentral gyrus are not tracked completely and WM fibers terminate abruptly as they approach the GM. Fiber tracking was terminated when the FA value was less than 0.15 and the turn angle was less than 60°. Fiber lengths were measured using DTI Studio v2.4. The percentage increase in the length of the fibers was also calculated. dTV was used for visualization of the nerve fibers since it directionally encodes the color of the fibers.

4.2 Results for the ex vivo studies

4.2.1 Diffusion Parameters (FA and ADC)

Data from the eight experiments on the fixed rhesus macaque brains were combined to study the effects of the application of long diffusion time to DTI tractography. The FA maps for three slices acquired during one of the experiments are shown in Figure 20.

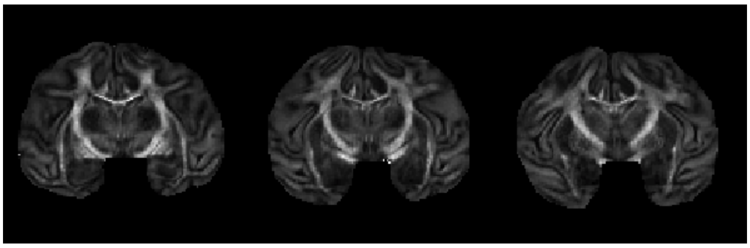

Figure 20: FA Maps of the Three Slices Acquired in One Experiment.

Figure 21 shows the FA values computed for the three imaging paradigms. The FA values obtained with DSE, STEAM48 and STEAM192 were 0.31 ± 0.02, 0.32 ± 0.03 and 0.35 ± 0.03 respectively. Thus, for STEAM192, the FA value measured in the WM was $11.5 \pm 5.0\%$ ($p < 0.05$) higher as compared to STEAM48 and greater by $11.2 \pm 5.2\%$ ($p < 0.05$) with respect to DSE. There was no significant change ($p = 0.2$) in the FA of the GM. The FA value measured by DSE, STEAM48 and STEAM192 in the GM, was 0.15 ± 0.01, 0.15 ± 0.02 and 0.16 ± 0.02 respectively.

ADC was also measured in the WM and the GM. With STEAM48, the ADC in the WM was calculated as 0.177×10^{-3} mm^2/s and with DSE, it was estimated at

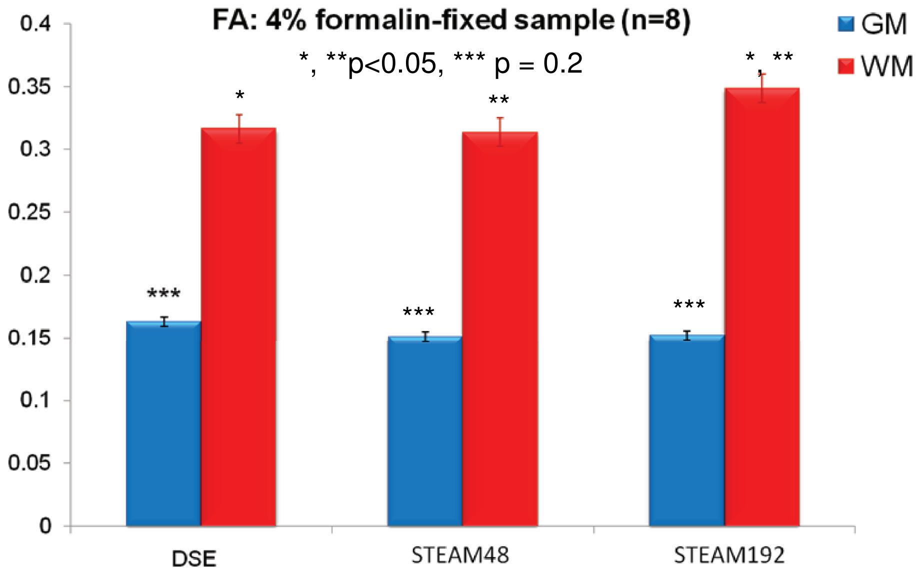

Figure 21: FA values in the WM (red) and the GM (blue): The FA value measured at t_{diff} = 192 ms in the WM was 11.5 ± 5.0% ($p < 0.05$) higher as compared to t_{diff} = 48 ms. It was also 11.2 ± 5.2% ($p < 0.05$) greater than FA obtained with the DSE sequence (t_{diff} = 45 ms). The GM values were not statistically different.

0.155 $\times 10^{-3}$ mm^2/s. The value of ADC with STEAM192 was 0.161 $\times 10^{-3}$ mm^2/s. In the STEAM sequence, the ADC of the WM decreased with increase in diffusion time. However, the ADC value shows a contradictory increase with t_{diff} when the STEAM192 and DSE (t_{diff} = 45 ms) are compared. This is because the residual cross-term interactions affect both the sequences differently as mentioned in Chapter 3. Instead, the ratio of $\frac{\lambda_1 \times 2}{\lambda_2 + \lambda_3}$ (ratio of parallel diffusivity to perpendicular diffusivity [72]) was calculated from the eigen values. This ratio was found to be 1.52 ± 0.08 in DSE, 1.53 ± 0.06 in STEAM48 and 1.62 ± 0.07 in STEAM192 which again confirms a heightened sensitivity to anisotropy at long diffusion time.

4.2.2 Tensor Evolution

To determine the nature of diffusion anisotropy that caused the increase in FA, three phase plots were obtained. A region of interest (ROI) was drawn to include the white matter tracts and the WM - GM regions. While planar diffusion increased only marginally in some ROIs, the diffusion was mostly linearly anisotropic at long

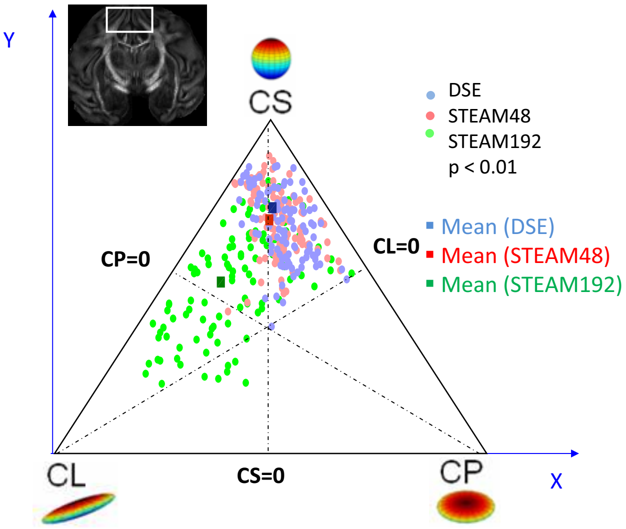

Figure 22: Three-Phase Plots: This three-phase plot depicts the geometry of diffusion in the area of the paracentral gyrus shown in the inset. The plot clearly shows that the diffusion was more linear at long t_{diff} of 192 (green scatter plot) ms as compared to the tensors obtained at the short t_{diff} using STEAM (red scatter plot) as well as DSE (blue scatter plot). Note also the scatter plot for DSE and STEAM48 is almost identical, proving that the increased linear diffusion anisotropy was not due to the use of the STEAM sequence. The dark red, blue and green squares represent the means of the three scatter plots.

diffusion time. One such example is shown in Figure 22.

Looking at the principal eigen vectors in this region (Figure 23), it can be seen that the tensors indeed, had a larger magnitude for the STEAM192 acquisition as compared to the short diffusion time acquisitions. The orientations of the tensors also are more coherent with those observed in adjacent voxels. The directional entropy, measured in this ROI was 2.03, 2.10 and 1.96 for DSE, STEAM48 and STEAM192 respectively.

DE was measured along the callosal fiber tract (CC) and the cortico-bulbar, cortico-pontine and cortico-striatal fiber bundles through the internal capsule (IC). The measurements are documented in Table 4. The *DE* in STEAM192 decreased by 18.1 ± 7.2% as compared to STEAM48 and 17.3 ± 6.3% as compared to DSE, in the corpus callosum. *DE* obtained in the IC with STEAM192 was 8.4 ± 1.3% less than the *DE* obtained with STEAM48. Further, comparison of *DE* in the internal capsule for the DSE and STEAM192 acquisitions showed that the DE reduced by 10.5 ± 1.2% for STEAM192.

Table 4: *Ex Vivo* Study: DE calculated along the callosal fiber tract (CC) and in the internal capsule (IC). The values represent mean ± standard deviation.

Acquisition	**CC**	**IC**
DSE	3.19 ± 0.11	2.44 ± 0.52
STEAM48	3.23 ± 0.08	2.38 ± 0.50
STEAM192	2.64 ± 0.29	2.19 ± 0.49

4.2.3 Connectivity and Tractography

Fast marching was implemented by placing a seed that would have probable connections in the cortico-striatal and cortico-pontine fiber tracts and the callosal fiber tract. For the result shown in Figure 24, the front propagation was terminated when the maximum connectivity metric was less than 0.5 times the maximum connectivity. Clearly the front propagated with STEAM192 traverses further towards the cortical surface in the paracentral region. In general, it can be seen that the connectivity front spans a greater area with STEAM192.

Finally, line propagation was performed using DTI Studio and dTV. Two seeds were placed, one in the corpus callosum and one in the internal capsule. Figure 25 shows the tractography results for the *ex vivo* rhesus brain. The fibers in the

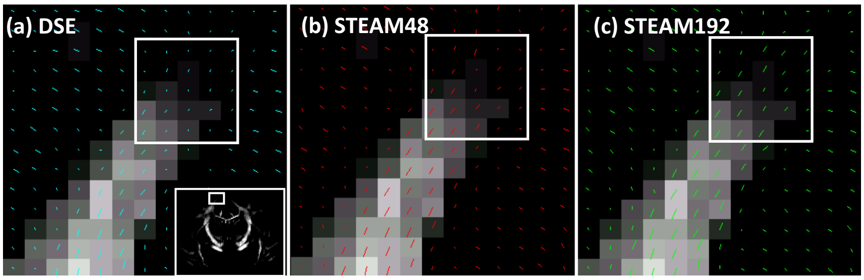

Figure 23: Tensor Evolution: The principal eigen vectors ϵ_1 are overlaid on the region of paracentral gyrus and precentral gyrus shown in the inset. It can be seen in the white box that the principal eigen vectors have a higher magnitude with STEAM192 (c) as compared to those obtained with DSE (a) and STEAM48 (b)

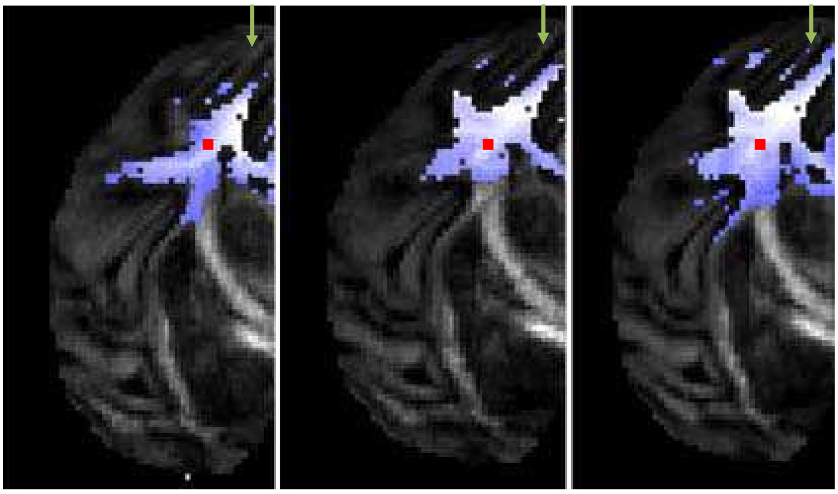

Figure 24: Connectivity Map using Fast Marching Technique. It can be seen that the front propagates further into the paracentral gyrus with STEAM192 as compared to STEAM48 and DSE indicating connectivity in the regions of less structural organization. The seed point is shown in red.

paracentral gyrus and the precentral gyrus are much longer in STEAM192. The fiber bundle in the internal also appears much thicker. Table 5 shows that the average fiber length, also increases in the entire brain volume with the use of long t_{diff}. It was observed that many more fibers, detected with STEAM192, terminated in the striatal regions when compared with those obtained with STEAM48 and DSE. However, the number of fibers is not used as a comparison metric. This is mainly because DTI is limited to the detection of one fiber in each voxel regardless of the voxel size. The number of fibers is dependent on the tensor estimated in each voxel and its orientation which determines the path that the fiber tract traverses.

Table 5: *Ex Vivo* Study, Tractography Outcome: Increase in fiber length calculated using DTI Studio v2.4 [28]. The values represent mean ± standard deviation.

Acquisition	**Corpus Callosum (CC)**	**Internal Capsule (IC)**	**Brain Volume**
STEAM48 vs. STEAM192	14.56 ± 5.83%	24.79 ± 6.89%	20.41 ± 13.92%
DSE vs. STEAM192	13.91 ± 9.93%	21.17 ± 10.38%	16.36 ± 9.16%

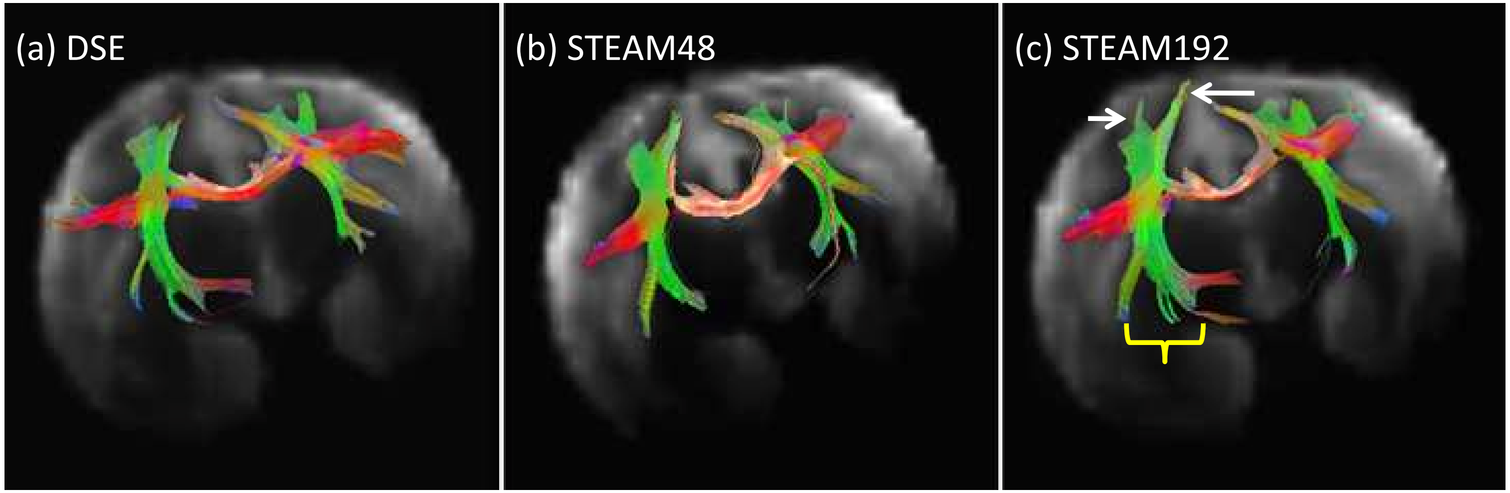

Figure 25: Tractography in *Ex Vivo* Sample: Seeds were placed in the corpus callosum and the internal capsule. Tractography results are shown for the DSE (a), STEAM48 (b) and STEAM192 (c) acquisitions. As pointed out in (c), the callosal fibers were tracked further into the cortical surface (shown by the white arrows). Additionally the fibers from the cortico-striatal and cortico-pontine fiber tracts in the internal capsule were much longer in striatal region shown by the yellow brace bracket. The tractography shown here is performed using dTV. [44]

4.3 Results for the in vivo studies

The above results proved that the application of DTI at longer diffusion times, indeed, improves the tractography outcome, by a potentially accurate sampling of the diffusion space in the tissue and by alleviating the effects of tensor averaging and IVOH. The imaging protocol was subsequently translated to perform *in vivo* studies in rhesus macaques. The acquisition time for each scan in the *ex vivo* experiment was about 0.5 hours. The maximum duration of the *in vivo* scans is approximately 3.5 hours. Therefore, the sequence was modified further and cross-term correction was implemented as mentioned in Chapter 3. Although, the *in vivo* studies have an advantage of a higher SNR due to the longer $T1$ and $T2$ relaxation times, and the reduced resolution of 1 mm × 1 mm × 1 mm, the total acquisition time restricts the number of averages that can be collected in an experiment. Five rhesus macaques were scanned in this study. Six experiments were conducted for each set of comparison: DSE vs. STEAM200 (Set 1) and STEAM50 vs. STEAM200 (Set 2). Analysis for the two sets follows next:

4.3.1 Diffusion Parameters (FA and ADC)

FA was measured in the WM and GM areas for DSE, STEAM50 and STEAM200. Figure 26 shows the comparison of FA calculated using DSE, STEAM50 and STEAM200. Figure 26(a) shows the fractional anisotropy obtained with STEAM50 and STEAM200. The FA values in the WM were 0.45 ± 0.04 with STEAM50 and 0.49 ± 0.04 using STEAM200. The FA in the GM remained unchanged ($p = 0.8$). In the second set of experiments, the white matter FA calculated by DSE was 0.44 ± 0.05 while the FA calculated by STEAM200 was 0.47 ± 0.04, thus establishing that FA in the WM increases with increase in t_{diff}.

The values for ADC, λ_1, λ_2, λ_3, and the ratio of parallel diffusivity to perpendicular diffusivity are shown in the Table 6. For reasons mentioned earlier, a comparison of

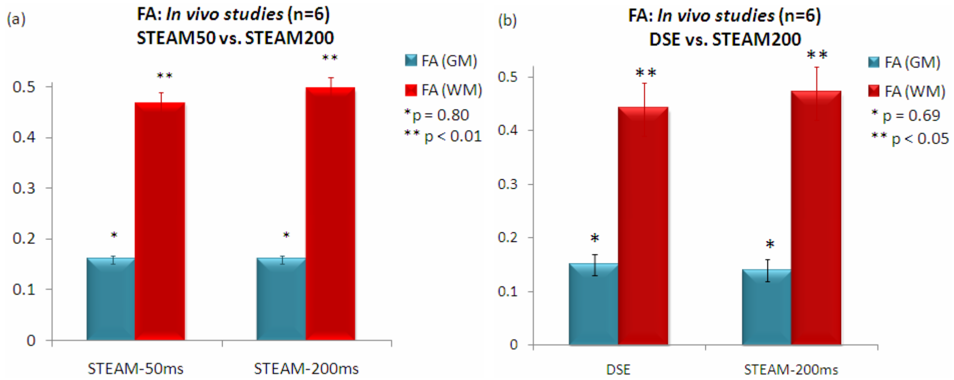

Figure 26: *In Vivo* Studies (FA of GM (blue) and WM (red):(a) Comparison of FA between STEAM50 and STEAM200. STEAM200 showed an increase of 6.03 ± 0.52 % ($p < 0.01$) over STEAM50. (b) In the second set, FA increased by 5.66 ± 0.06 % ($p < 0.05$) when STEAM200 was used instead of DSE.

ADC values obtained with DSE, STEAM50 and STEAM200 was not made.

Table 6: *In Vivo* Study: ADC and Eigen values for DSE, STEAM50 and STEAM200. All values represent mean ± standard deviation × 10^{-3} mm^2/s. The ratio has no units.

Parameter	**Set 1**		**Set 2**	
	STEAM50	**STEAM200**	**DSE**	**STEAM200**
D	0.73 ± 0.04	0.67 ± 0.05	0.79 ± 0.05	0.67 ± 0.05
λ_1	1.10 ± 0.08	1.06 ± 0.08	1.22 ± 0.08	1.05 ± 0.09
λ_2	0.66 ± 0.04	0.60 ± 0.04	0.69 ± 0.04	0.59 ± 0.04
λ_3	0.41 ± 0.03	0.36 ± 0.03	0.46 ± 0.03	0.37 ± 0.03
$\frac{\lambda_1 \times 2}{\lambda_2+\lambda_3}$	2.07 ± 0.07	2.20 ± 0.07	2.10 ± 0.08	2.20 ± 0.08

4.3.2 Tensor Evolution

Analogous to the *ex vivo* studies, the three-phase plots showed an increase in linear diffusion for the selected ROIs. Mean of the scatter-plot obtained at the long t_{diff} value of 200 ms was calculated and was found to be significantly ($p < 0.001$, Kolmogorov-Smirnov test) different from the mean of the scatter plot at the short t_{diff} of approximately 45 ms (Figure 27).

Figure 28(a) compares the tensors obtained with STEAM50 and STEAM200 in the paracentral gyrus. Similar to the *ex vivo* results, the primary eigen vectors and hence tensor magnitudes are much larger for the STEAM200 sequence in comparison

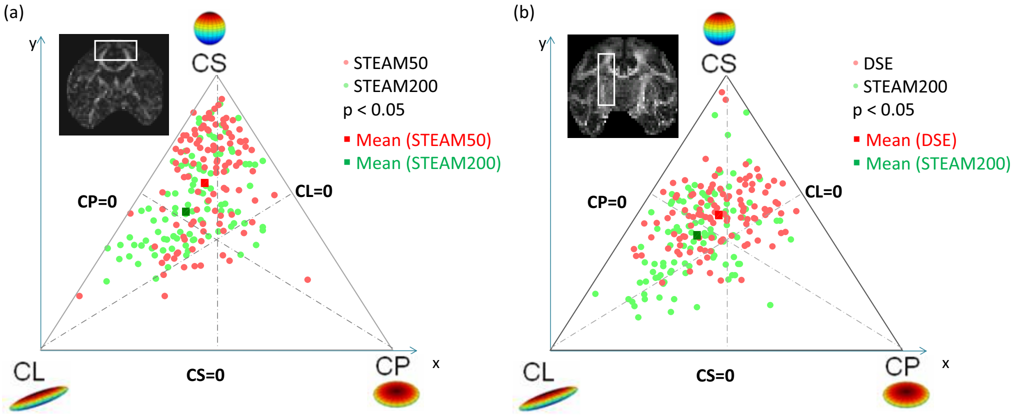

Figure 27: Three-phase plots in the *In Vivo* Study. (a) Pink dots represent the diffusion anisotropy obtained at $t_{diff} = 50$ ms and the pale green dots represent anisotropy at $t_{diff} = 200$ ms obtained with the STEAM sequence in the paracentral gyrus. The respective mean values (red - STEAM50, green - STEAM200) are significantly ($p < 0.001$) different and indicate that CL increased when STEAM200 was used. (b) shows the scatter plot for DSE (pink dots) and STEAM200 (pale green dots). Again the use of STEAM200 increased linear anisotropic diffusion as compared to DSE ($t_{diff} = 47$ ms

with the principal eigen vectors obtained with STEAM50. Similar results are obtained when tensor maps are calculated and compared for the DSE and STEAM200 acquisitions. Figure 28(b) also shows increased coherence in the tensor orientation near the striatal region.

The *DE* was calculated in the callosal fiber tract and the internal capsule (Table 7). Comparison of the directional entropy, calculated by STEAM50 and STEAM200, revealed that *DE* decreased by 17.06 ± 4.04% in the CC and by 9.79 ± 2.21% in the IC with STEAM200 when compared to STEAM50. In the second set of comparison, *DE* decreased by 12.16 ± 1.62% with STEAM200 with respect to DSE in the CC and by 14.88 ± 2.57% in the IC. Again, the decreased *DE* confirms that the tensors in the adjacent voxels along a fiber tract are more co-linear at long t_{diff} than at short diffusion time.

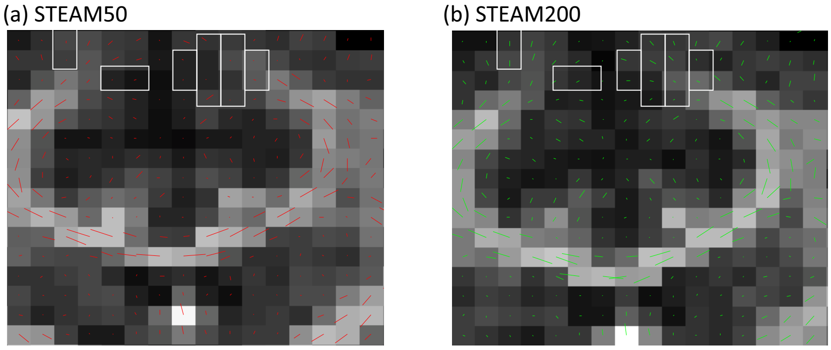

(a) STEAM50

(b) STEAM200

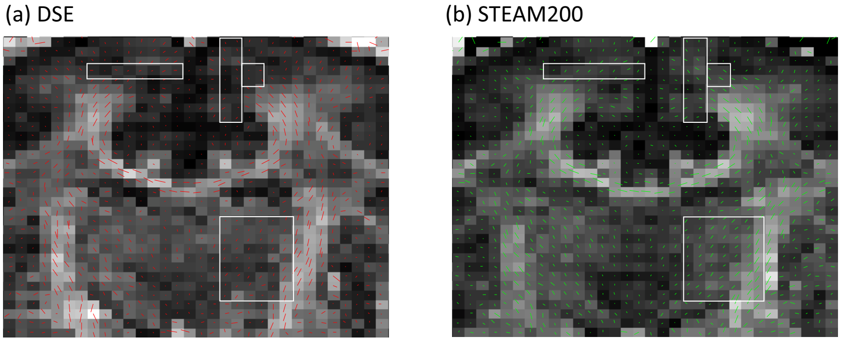

(a) DSE

(b) STEAM200

Figure 28: Tensor Evolution: The first row compares the principal eigen vector plots, obtained in the paracentral gyrus with STEAM50 and STEAM200 and the second row compares the plots for DSE and STEAM200. The white squares show regions where STEAM200 estimated longer and coherent tensors.

Table 7: *In Vivo* Study: Directional Entropy measures in the corpus callosum and the internal capsule. All values represent mean ± standard deviation.

Region	**Set 1**		**Set 2**	
	STEAM50	**STEAM200**	**DSE**	**STEAM200**
Corpus Callosum (CC)	2.33 ± 0.51	1.93 ± 0.48	2.98 ± 0.49	2.60 ± 0.48
Internal Capsule (IC)	2.00 ± 0.54	1.80 ± 0.52	2.46 ± 0.48	2.10 ± 0.60

4.3.3 Connectivity and Tractography

Fast Marching Tractography (FMT) was performed on the *in vivo* data that was acquired for the three sequence protocols. Again, the front was allowed to propagate until it spread into GM regions or outside the brain tissue. Figure 29 shows the outcome of FMT. The cut-off threshold for the *in vivo* studies was 0.35 of the maximum connectivity.

Line propagation was performed next. The results are shown in Figure 30. The

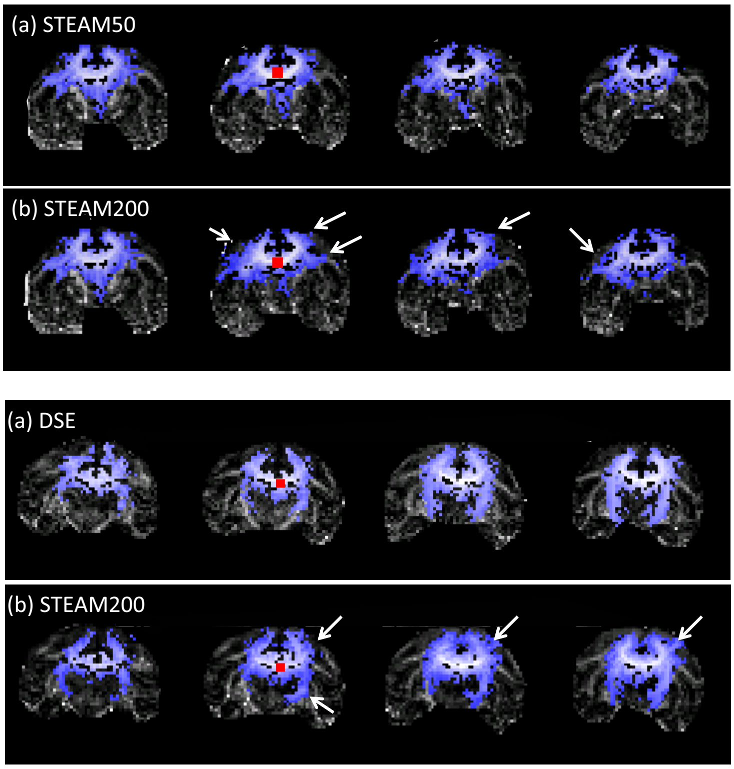

Figure 29: Fast Marching in *In Vivo* Experiments: The first row shows the fast marching connectivity profiles obtained for STEAM50 and STEAM200 when the seed was placed in the corpus callosum. It can be seen (white arrows) that STEAM200 shows more extensive connections when compared to STEAM50. In another experiment, similar results were obtained when fast marching was implemented and comparison was made between in DSE and STEAM200.

first row compares fibers tracked by DSE and STEAM200 while the second row compares tractography outcome of STEAM50 and STEAM200. The figures clearly show that the nerve fibers from the CC and the cortico-pontine tracts traced in the frontal lobe are more abundant and longer at a long t_{diff} of 200 ms as compared to a t_{diff} of $\approx$ 47 ms. Percentage increase in the length of the fibers is documented in Table 8.

Comparison of the *ex vivo* and the *in vivo* results further shows that the improvement due to the use of long diffusion time for DTI tractography was more pronounced in the *ex vivo* studies. Possible reasons for this difference are outlined below:

- Tissue Properties: Studies reveal that the ADC in formalin fixed *ex vivo* brain samples decreases significantly [72, 14] by about 50% - 75% as compared to the

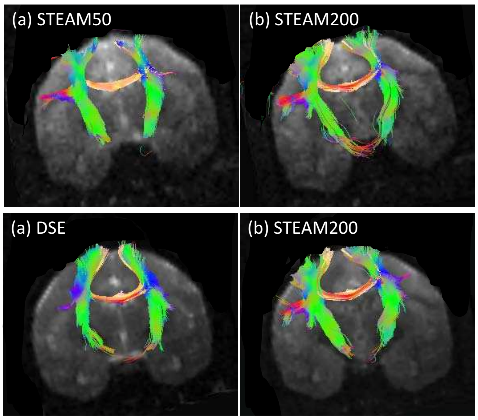

Figure 30: Line Propagation, *In Vivo* Studies: The first row compares line propagation outcome for STEAM50 and STEAM200. The fibers in the paracentral gyrus and the precentral gyrus (frontal lobe) are much more abundant and longer in STEAM200 as against STEAM50. Similar results were obtained in the frontal lobe, when DSE and STEAM200 was compared.

ADC of water in the brain tissue *in vivo*. The $T1$ and $T2$ relaxation parameters change significantly following fixation due to the reduced water content and tissue shrinkage. Furthermore, the pulse sequences themselves introduce some $T1$ and $T2$ weighting in the tissue. The relative population of water species with the longer and shorter $T2$ does not remain the same after fixation and the TR and TE cannot be adjusted well enough to compensate for these changes, due to the limitations of the gradient fields.

Although the reason for the reduced ADC is unclear, Sun *et al.* [72] believe that formalin fixation affects the lipid composition in the myelin sheaths thereby increasing the barriers encountered by the diffusing water molecules. The ADC

Table 8: *In Vivo* Study: Percentage increase in fiber lengths

Acquisition	**Corpus Callosum (CC)**	**Internal Capsule (IC)**	**Brain Volume**
STEAM50 vs. STEAM200	10.10 ± 2.89%	7.34 ± 2.77%	8.52 ± 3.62%
DSE vs. STEAM200	6.24 ± 1.46%	11.44 ± 4.68%	6.32 ± 2.16%

of a normal un-fixed brain is $\approx 0.76 \times 10^{-3}$ mm^2/s and a t_{diff} of 48 ms samples a diffusion space of $\approx$ 15 μm. However for the fixed tissue, the 3D distance traversed by water with an ADC of $\approx 0.15 \times 10^{-3}$ mm^2/s is $\approx$ 6 μm. Hence it is likely that all the restrictive boundaries are not sampled at a short t_{diff} of 48 ms in a fixed sample.

- b Value: The imaging parameters are significantly different for the two studies, especially the b value. The b value for *ex vivo* studies was 1700 s/mm^2 while that in the *in vivo* studies was 1200 s/mm^2. The higher b value was necessary to produce enough contrast between the b_0 image and the diffusion weighted image to ensure correct estimation of the diffusion parameters. However, a higher b-value also increases the sensitivity of DTI to diffusion anisotropy [1, 82].

- Resolution: Diffusion tensor estimation in DTI is greatly affected by the image resolution. At higher resolution, the low SNR causes an overestimation of the DTI parameters and at a lower and poorer resolution, DTI parameters are affected by partial volume effect. The *ex vivo* experiments were acquired at a high resolution of 0.54 mm × 0.54 mm × 2 mm while the *in vivo* data was acquired at a poorer resolution of 1 mm × 1 mm × 1 mm. Additionally, in this study the SNR of the *ex vivo* brain images was higher than that obtained *in vivo* due to the large number of averages possible in that study.

  A lower resolution yields large voxels containing different tissue components such as the WM, GM and the cerebrospinal fluid (CSF) giving rise to partial volume effects . Partial voluming significantly alters the calculations of FA, CL and CP [1]. The effect of partial volume greatly depends on the underlying tensor orientations and volume fraction for each tissue component and makes the rotationally independent parameters such as FA and ADC to be dependent on the rotational orientation. This rotational dependence has been observed greatly in the cingulum (anterior and posterior), pyramidal tracts, the middle cerebral peduncle and the corpus callosum. Rotational dependence of DTI parameters was shown to reduce with increase in the resolution [1]. Further the standard deviation of the FA becomes larger at lower resolutions due to the effect of partial voluming [32]. Thus, the effect of partial volume is higher in the *in vivo* studies due to the low resolution causing an underestimation of the FA thereby limiting the improvement seen due to the application of long diffusion time.

- Other: A reduced SNR has been shown to cause an overestimation of the FA values [82]. For the *in vivo* studies, although the voxel size was larger in comparison to the voxel size used for *ex vivo* studies, the SNR value was not as high as the one obtained *ex vivo*.

CHAPTER V

VALIDATION OF DTI TRACTOGRAPHY

Diffusion tensor imaging has revolutionized the non-invasive study of tissue microstructure and has provided a detailed insight into the structure of the brain. However, the validation of the information obtained from DTI images remains to be investigated. This is particularly important in the diagnosis and evaluation of white matter disorders such as Alzheimer's Disease and multiple sclerosis, where there is significant variability across affected individuals.

Phantoms with known geometrical arrangements are being designed to test the fidelity of DTI tractography [81, 41]. But it is difficult to reproduce the tissue structure and emulate the ongoing active and passive processes that occur in a tissue. Besides, the exact mechanism for the dependency of diffusion anisotropy on diffusion time is yet unknown. However, recent studies use complementary MR techniques to validate the fiber tractography obtained using DTI. For example, Lin *et al.* successfully validated the accuracy of DTI in delineating the optic tract in mice with a simultaneous acquisition of Manganese Enhanced MRI (MEMRI) [37] .

DTI tractography in animals has been limited to the study of small animals and rodents [86]. Very few studies have been done in non-human primates. However, nerve connections in the rhesus brain have been outlined in great detail using histology, autoradiography and staining techniques [19, 88, 71]. One such neural pathway is the visual pathway [29, 30]. Fast marching technique was used to successfully delineate the optic radiation originating from the LGN in the rhesus macaque by Parker *et al.* [60]. The study was however, conducted at a much lower resolution (in-plane resolution: 2.2 mm × 2.2 mm) and suffered from partial volume effects. No results were shown for the optic tract. In this study, the extensive documentation available on the morphology of the optic tract in non-human primates was used to choose the tract for validating the results obtained using DTI at long diffusion time [29, 71].

In the previous chapters, it has been proved that the use of long diffusion time for DTI tractography provides longer fiber tracts as compared to conventional DTI. This chapter verifies if the fibers tracked using DTI at long t_{diff} are more accurate and conform to the well- documented anatomy of the rhesus brain. For this purpose, tracking was performed in the optic tract using the standard DSE sequence at t_{diff} = 45 ms and STEAM192 at t_{diff} = 192 ms. Comparison between STEAM48 and STEAM192 was not made since the earlier *ex vivo* studies indicate that the DTI outcome with STEAM48 and DSE is similar. Further, the DSE sequence is the most popular method used for DTI tractography and comparison of the DTI ouctome, using STEAM192, would provide us an idea of the improvement in tractoraphy, observed with STEAM192, with respect to the current standards.

5.1 Visual System Tractography

The visual system forms an important component of the central nervous system which allows an organism to see objects and perceive their depth and motion. The visual system consists of the eye (retina), the optic nerve, optic chiasm, optic tract, lateral geniculate nucleus (LGN) , the optic radiation, primary visual cortex and the associate visual cortices (Figure 31). The photoreceptor cells in the retina receive light and transmit the sensory input to the bipolar cells they synapse with. Most of the retinal axons terminate in the LGN. The LGN consists of 6 layers of cell bodies [31, 30] that are separated by the intralaminar layers of the axons and the dendrites and is a structure in the thalamus (midbrain). The LGN also consists of a number of nerve fibers that project to the visual cortex and the visual association cortex via the optic radiation. The numerous fibers and fiber crossings in the LGN, make it difficult to tract the retinal projections that reach it via the chiasm [27] using DTI.

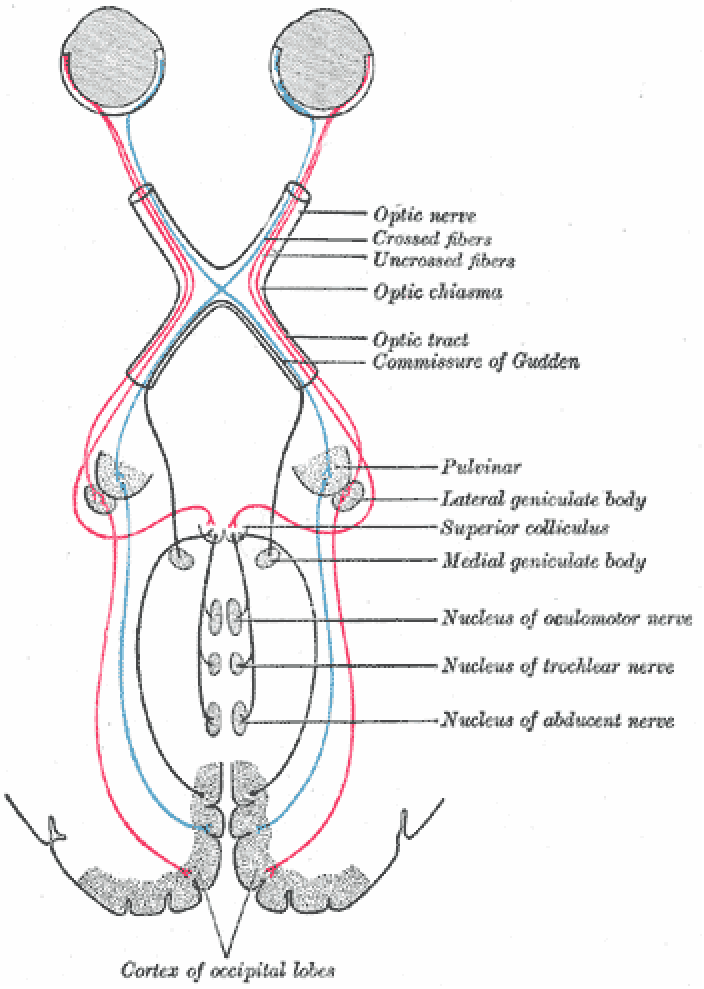

Figure 31: The Mammalian Visual System. Taken from [21]

The study by Lin *et al.* [37] revealed that the axonal projections tracked by DTI stopped short of the LGN due to the random tensor orientation in the LGN. Few nerve fibers that reach the LGN continue to the Superior Colliculus (SC). No tracking was performed to detect nerve fibers that project to the superior colliculus from the retina via the LGN. Another study that compared fiber orientations using DTI and Diffusion Spectrum Imaging (DSI) in the optic tract revealed that the error in the determining the correct fiber orientation in the superior colliculus was significantly higher [38] due to the presence of multiple fiber orientation also referred to as IVOH.

In this study, an attempt was made to tract the optic projections in the chiasm from the retina to the LGN and the SC. Since the *ex vivo* study already established that the STEAM sequence to implement DTI at long diffusion time improves tractography in comparison to DTI at short diffusion time, regardless of a STEAM or DSE implementation, only the standard sequence DSE at short t_{diff}, and STEAM at long t_{diff} were compared. The data was compared to available histological data and to the anatomical data collected during the acquisitions. Details of the study follow next.

5.2 Experiment Design

5.2.1 Setup

For this comparative study, fixed rhesus macaque brain samples were used. The samples were washed in water and immersed in water containing 0.018 mg/ml of MIONs to prevent Gibbs Ringing. Geometric averaging was used for cross-term correction. The slice selection was based on the $T2$-weighted anatomical data that was collected prior to the DTI study. The imaging protocol was identical to the one used for the *ex vivo* studies. Only, 7 axial slices were collected to cover the entire optic tract. Since the slice thickness was too high (2 mm), there was a possibility that the detailed structure of the LGN would not be detected, so sagittal slices were acquired in one of the experiments to capture the dolphin shaped structure of the LGN. Seven experiments were conducted on two fixed brains samples.

Anatomical data was acquired using the same imaging parameters as the *ex vivo* study. The anatomical images and the corresponding color coded and directionally encoded maps for the acquired slices are shown here (Figure 32).

5.2.2 FA and Tensor Evolution

Fractional anisotropy was measured along the optic tract. The FA value measured by DSE at $t_{diff} = 47$ ms, was 0.49 ± 0.07 while FA calculated by STEAM192 was 0.54 ± 0.08, corresponding to an increase of $8.69 \pm 1.78\%$. This increase in FA translated

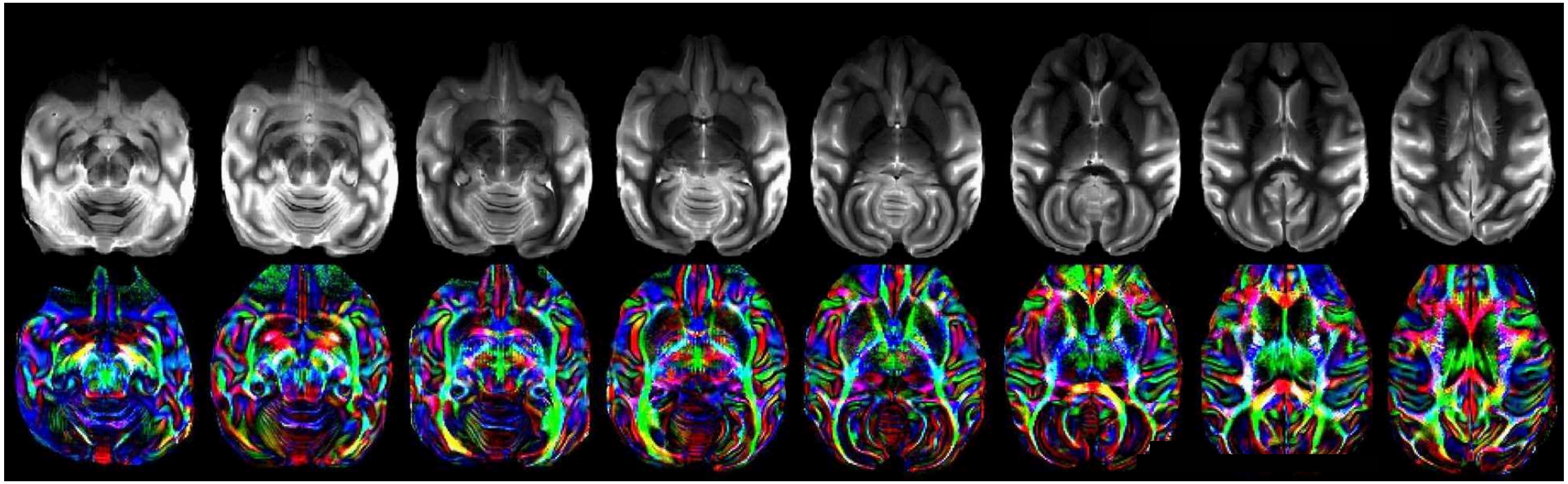

Figure 32: Top row: $T1$ weighted images of the slices containing the optic tract. The bottom row show the color coded FA maps for the corresponding slices. (The red color represent fibers traversing horizontally from left to right or right to left, green color represents fibers that go from top to bottom or vice versa and blue represent fibers that come in or go out of the plane of the image.

to increased magnitude of the diffusion tensors as shown next.

Plots superimposing the principal eigen vectors on the FA maps were evaluated across the different slices. Figure 33 shows the first two slices. Similar to the observations in the *ex vivo* and *in vivo* studies, it can be seen that the tensor orientations in the first slice that represents the start of the optic tract are slightly longer with STEAM192. More prominently, when the tract advances toward the LGN in the second slice bottom row, the FA falls significantly in the optic tract. The eigen vectors obtained with DSE are not as prominent or coherent as those seen in the STEAM192 acquisition. Similarly in the fifth slice containing the SC, the tensors obtained with STEAM192 are much longer than those obtained from the DSE acquisition.

Directional entropy was measured along the optic tract. In the DSE acquisition, DE was 2.87 ± 0.58 and in the STEAM192 sequence, DE was 2.70 ± 0.70. The decreased DE confirms the increased tensor coherence seen in Figures 33 and 34.

5.2.3 DTI Tractography

Fast marching and line propagation was performed in the optic tract. The DTI data was compared with the histological data and MR atlas for humans and monkeys and the LGN and the SC were located in the $T1$-weighted anatomical images for reference. For fast marching an ROI was placed on the optic tract between the chiasm and the LGN. As can be seen in the figure, the connectivity profile propagates almost vertically through the four slices shown in Figure 35. The front propagated by STEAM192 is more similar to the anatomical arrangement of the optic tract in that it traverses laterally away from the chiasm as it propagates through the four slices. The front curves inwards (slice 3) to terminate in the LGN and further shows diffuse connectivity to the SC.

For the line propagation technique, two region tractography was performed with one region of interest (ROI), placed in the optic tract just after the chiasm and the

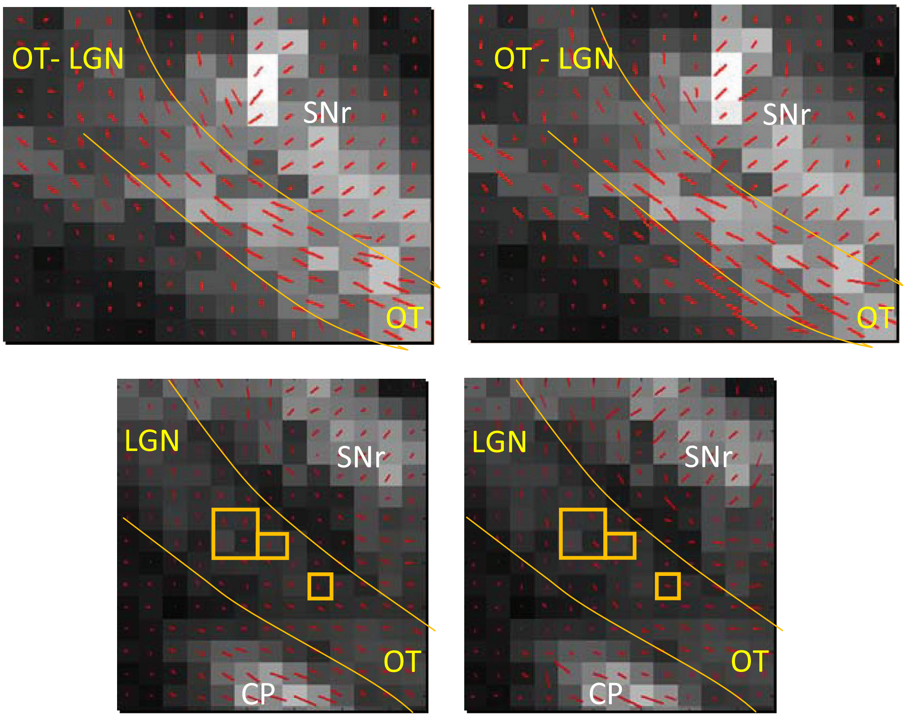

DSE **STEAM192**

Figure 33: Tensor Plots in the First and the Second Slices: The first slice (top row) shows the tensors as the inception of the optic tract. The second slice (bottom row) depicts the tensors in the optic tract as it reached the LGN. OT: Optic Tract, SNr: Substantia Nigra

other ROI was placed in the SC, based on their location in the anatomical images. The number of fibers tracked between the 2 regions were calculated using dTV. While DSE did not track any fibers when two-region tractography was used STEAM192 delineated 20 ± 8 fibers. The results shown in Figure 36 are procured using a single ROI placed on the optic tract. The optic fibers, tracked by STEAM192 conformed with the anatomical description of the tract. After tractography, the images were registered to the anatomical $T1$-weighted images and superimposed on the anatomy to verify the accuracy of fiber tracking. The imaged brain volume was rendered in 3D and the optic tracts were visualized in the brain volume. Image registration was performed using a customized code for image registration [1] using the MATLAB image

---

[1] Image registration is the process of establishing a point-by-point correspondence between two

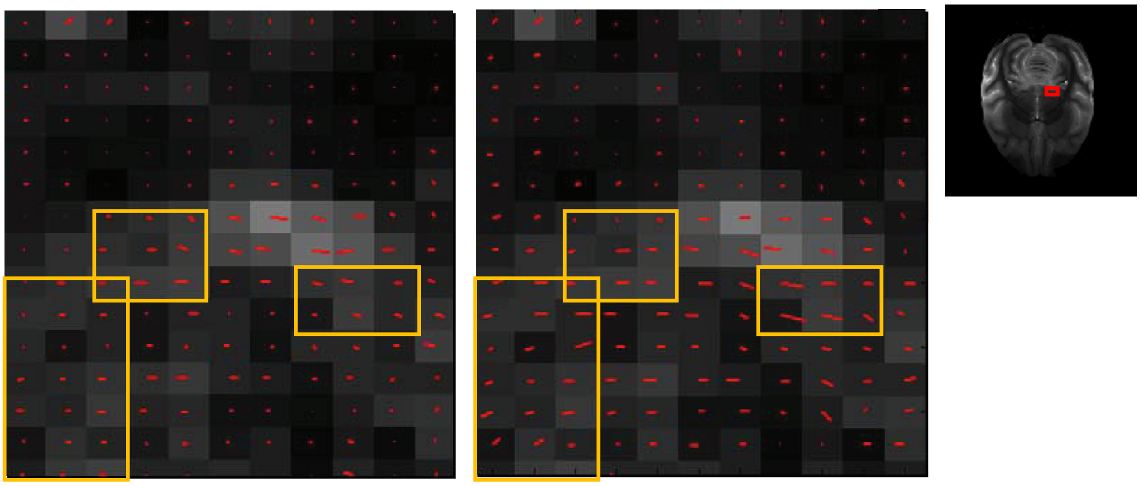

DSE **STEAM192**

Figure 34: Tensor Plots in the Fifth Slice: The slice contains the superior colliculus where some of the retinal axons terminate. The region depicted is shown by a red square on the right. OT: Optic Tract, SNr: Substantia Nigra, CP: Cerebral Peduncle

processing toolbox. At least 6 points were selected to register the anatomical dataset to the DTI data. Linear registration was performed to determine the location of the fibers relative to the anatomy. DSE tracks fibers from the chiasm to the LGN but the fibers do not curve inwards to terminate in the superior colliculus.

Apart from the retinal fibers that project to the superior colliculus via the LGN, there is another small neural pathway, the tecto-geniculate pathway that contains nerve fibers that originate in the LGN and terminate in the SC. This pathway cannot be distinguished from the optic tract using DTI. Thus, the number or length of fibers that truly belong to the optic tract cannot be estimated. This failure of DTI to differentiate the two pathways therefore, limits the use of the optic tract for validation. Yet, as shown in this study, it proves to be an excellent choice for testing the accuracy of fiber tracking.

---

images.

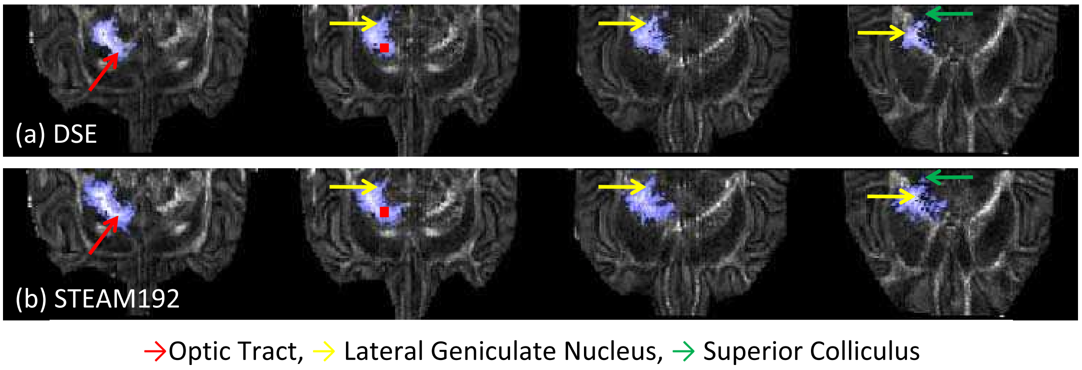

Figure 35: Fast Marching in the Optic Tract: Top row shows the four slices and the connectivity front for DSE (a) and the bottom row shows the front for STEAM192 (b).

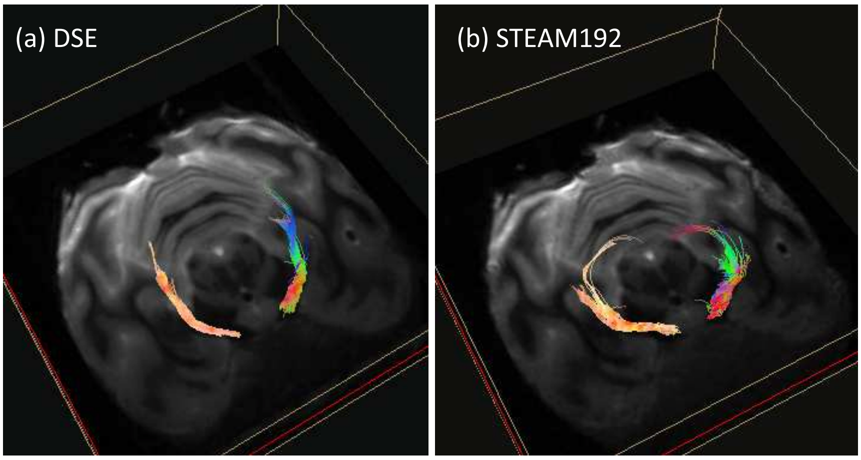

Figure 36: Line Propagation in the Optic Tract: Fibers tracked in optic tract by (a)DSE and (b) STEAM192

CHAPTER VI

CONCLUSION

Diffusion tensor imaging is a powerful tool to study nerve tissue ultra-structure by sampling the diffusion of water molecules in the tissue. The brain tissue mainly comprises of the white matter and grey matter. The highly restrictive and non-uniform diffusion in the white matter and the nearly uniform diffusion in the grey matter provides the necessary diffusion based contrast for DTI. Additionally, DTI also provides directional information to interpret the orientation of the nerve fibers in the white matter. DTI measurements depend on the application of a pair of diffusion sensitizing gradients for a preset duration, t_{diff}. The commonly used value of t_{diff} is approximately 50 ms. Following Einstein's equation, this duration is sufficient to probe a diffusion space of about 15 μm - sufficient to probe the intra-cellular and extra-cellular space in the brain tissue. However, previous studies show that the diffusion anisotropy is dependent on the diffusion time.

This study was based on the hypothesis that use of a longer diffusion time for DTI tractography would increase the sensitivity of the technique to diffusion anisotropy, allowing a more accurate estimation of the tissue geometry. The anatomical similarity in the brain structure of humans and non-human primates makes non-human primates, excellent models for studying neurology and neuropathology. This work, therefore, comprised of evaluation of the effects of applying a long diffusion time to DTI tractography in rhesus macaques.

Conventional spin echo sequences used for diffusion weighted imaging cannot be used to achieve a higher value of t_{diff}. The sequences are restrained by $T2$ signal decay and the consequent loss in SNR. A STEAM-EPI sequence was customized for DTI, thereby allowing the application of long t_{diff} in DTI at a short TE. The STEAM sequence inherently has a lower SNR since only half the magnetization is used for the MR signal. The loss in SNR is partially recovered by the shorter TE allowed by STEAM. Indeed, the SNR in STEAM48 was higher than DSE in the fixed brain samples and similar in the *in vivo* studies. Comparison of STEAM192 was performed against STEAM48 and the DSE sequence. This was especially necessary, since the DSE sequence provides a $T2$ weighted image output while the image obtained with the STEAM sequence is $T1$ and $T2$ weighted. Further, since the $T1$ and $T2$ values of the GM are larger than those of the WM, it is likely that the diffusion weighted images show lesser signal attenuation in the GM, therebye enhancing the GM tissue signal intensity as compared to the WM.

The ex vivo and *in vivo* studies show that the by employing a long t_{diff} for DTI, the FA in the white matter and the white-gray matter interfaces increased significantly. The three-phase plots facilitate a geometrical interpretation of diffusion. Application of long diffusion time skewed the plots towards linearly anisotropic diffusion, indicating the availability of more rank 1 tensors that provide a dominant direction for the purpose of fiber tractography. The tensor plots, obtained by superimposing the principal eigen vector ϵ_1 on the FA maps, showed an increase in the magnitude of ϵ_1 at long diffusion time.

Local tissue arrangement is similar and is reflected by the similarity in the orientation of the diffusion tensors in adjacent voxels. It is believed that the use of long diffusion time improves the accuracy of the tensors. If the diffusion space in the tissue were not sampled enough at the conventional value of diffusion time, the tensor orientations would be more varied. On the other hand, if the sampling was indeed accurate at long diffusion time, the tensor orientations would be more collinear. Directional Entropy (DE) was used to evaluate the increased coherence/ collinearity amongst neighboring tensors along a fiber tract. As expected, DE was shown to have significantly decreased with the use of long t_{diff}.

Next, fast marching tractography was performed on the acquired DTI datasets. This energy minimization technique is considered more robust as compared to the line propagation techniques that are used for fiber tractography. It was observed that the fronts, propagated for the STEAM acquisition at long diffusion time, showed a larger area of connectivity. These fronts extended further into the GM-WM interfaces of cortex, especially in the paracentral gyrus, precentral gyrus, the striatal region and the optic tract of the brain. The advantage of this method can be clearly seen in the validation of fiber tractography in the optic tract. Although the STEAM192 has a larger area of connectivity in the optic tract as compared to DSE, DSE also shows some connectivity to the superior colliculus. However when line propagation was employed for deterministic tractography, the fibers delineated using DSE, did not terminate in the superior colliculus. Instead the fibers continued towards the optic radiation. One possible reason is because of the tensor averaging in the region of the lateral geniculate nucleus and the superior colliculus due to the presence of fiber crossings. Since line propagation relies only on independent voxel information, the fiber tract failed to detect the axonal projections to SC.

Fiber tracking was performed using DTIStudio and dTV. ROIs were placed in the corpus callosum and the internal capsule. The nerve fibers, delineated for DTI at long diffusion time, were longer than the nerve fibers tracked for DTI at short diffusion time. More callosal fibers terminate at the cortical surface when long diffusion time was used. Similarly more fiber branches from the cortico-pontine and cortico-bulbar tracts in the internal capsule are tracked in the precentral gyrus. Also the terminations of the cortico-striatal fibers are more pronounced for DTI at long t_{diff}. To ensure accurate tracking of the optic tract (*ex vivo*), two-ROI tracking was performed to determine if a thin bundle of fibers from the retina that terminates in the SC could be detected. This was possible only for the STEAM192 sequence. The number of fibers is not considered a reliable measure for DTI analysis . However in this case, it was used for a rough comparative evaluation of DSE and STEAM192. While tractography with DSE failed to track any fibers with the 2-ROI tracking, with STEAM192, 20 ± 8 fibers were tracked implying the increased accuracy of STEAM192. One ROI tracking was, therefore performed to compare the optical fibers obtained using DSE and STEAM192.

All the observations above prove that DTI at long diffusion time indeed improved the sensitivity of the technique to diffusion anisotropy and thereby improved tractography. As detailed in Chapter 4, the improvement was more pronounced in the *ex vivo* studies than in the *in vivo* studies due to the higher b value, higher resolution, and lower ADC in the *ex vivo* study. Although the exact mechanism for this improvement is yet to be investigated, it is believed that the diffusion space in the tissue is better sampled at long diffusion time. A larger number of diffusing water molecules encounter boundaries, thus fine-tuning the probability distribution function of diffusion and providing more accurate tensor orientations. The heightened FA and accuracy of the tensors subsequently improves the outcome of fiber tractography.

As mentioned above, the exact mechanism, responsible for this improvement has not yet been determined. Nonetheless, this mechanism was speculated and explained in Chapter 3 and can be considered as a combination of increased sampling of the diffusion space and reduced effect of IVOH. There have been studies [4, 3] that explore diffusion as a composite model of two independent types of diffusion; restricted and hindered each weighted by their volume fraction. This principle cannot be applied to DTI because DTI models the diffusion process as a Gaussian process and furnishes an average of all diffusion while, on the other hand, restricted diffusion is considered to be non-Gaussian. However, the composite model offers a simple way of speculating the factors that affect the diffusion process.

Restricted diffusion is the diffusion in the axoplasm (intra-axonal) and not between the layers of the myelin sheath and is relatively slower than hindered diffusion. Hindered diffusion refers to the extra-axonal part of diffusion. About 70% of the DTI signal is assumed to be due to hindered diffusion [4]. An example of such a hindered diffusion can be the diffusion in the ECM. The composition of ECM has been shown to obstruct diffusion across the axonal fibers in the spinal cord [58]. Wu *et al.* [84] estimated that the restricted diffusion coefficient in the WM in humans is 0.14 ± 0.11 mm^2/s and the hindered diffusion coefficient was 0.99 ± 0.35 mm^2/s. In the GM, restricted diffusion coefficient was reported as 0.37 ± 0.17 mm^2/s and hindered diffusion coefficient was 1.07 ± 0.45 mm^2/s. Assaf *et al.* show that the restricted diffusion is highly directional (anisotropic) while the hindered diffusion is comparatively less anisotropic (See Figure 37). Diffusion represented by restricted diffusion is like a toothpick and represents the non-Gaussian part of diffusion. The ellipsoid represented by hindered diffusion is similar to the diffusion ellipsoid obtained in conventional DTI and represents the Gaussian part of diffusion. Further, they [4] showed that diffusion imaging is more sensitive to hindered diffusion at smaller b values and to restricted diffusion at higher b values. It is conjectured that the use of long diffusion time increases the contribution of the slow restricted diffusion and increases the sensitivity of the technique to diffusion anisotropy. Additionally, the hindered diffusion may also become more anisotropic at long diffusion time.

It is important to note that the interaction of the two compartments; intra-axonal and extra axonal; is not accounted for in this model since it is considered to be a slow exchange process [5, 61]. This slow exchange, if consequential, will undermine the effect diffusion anisotropy, at long diffusion time. This is because the exchange occurs perpendicular to the axonal fibers and increased perpendicular diffusivity, thereby decreasing FA.

6.1 Future Directions

This study shows the feasibility of DTI at long diffusion time for *in vivo* studies in rhesus macaques. The results documented in Chapters 4 and 5 prove that the use of long diffusion time for DTI tractography undoubtedly improves tractography and hence the technique could potentially improve tractography in humans. It is important, however, to note that *in vivo* studies in non-human primates last upto 4 hours. Human scans last for approximately 1.5 hours. The STEAM-EPI sequence may need further modification to facilitate DTI at long diffusion time in humans.

Nair et. al [54], showed that the application of DTI at long diffusion time in myelin deficient *shiverer* mice increased the diffusion based contrast. The technique can therefore, be used to improve the sensitivity of DTI to other neuro-pathological disorders associated with neural tissue degradation. A combination of DTI at long diffusion time with a high *b*-value acquisition may further heighten the sensitivity of DTI to diffusion anisotropy in the diseased tissue.

DTI is greatly limited by its inability to detect multiple fiber orientations. It may be possible to detect the presence of multiple fiber bundles in the same voxel by sampling it at very short and very long diffusion times. It is likely that a voxel contains two populations of WM fibers with distinct orientations and each diffusion time may preferentially sample one fiber bundle over the other. Of course, a voxel containing equal populations of two distinct fiber bundles cannot be resolved with DTI. Newer methods such as the advanced fast marching technique use the complete

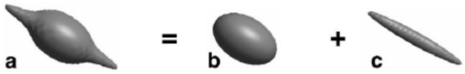

Figure 37: Composite Diffusivity Model: Diffusion (a) comprises of two processes, restricted diffusion (b) and hindered diffusion (c). Restricted diffusion forms the non-Gaussian part of diffusion, represented by a toothpick, while hindered diffusion represents the Gaussian part that is represented by a diffusion ellipsoid, similar to the one obtained in DTI. Reproduced from [4]

tensor information i.e., all the three eigen vectors $(\epsilon_1, \epsilon_2, \epsilon_3)$ in combination with the geometric measures of diffusion to determine fiber branching. DTI at long diffusion time could be combined with advanced fast marching technique to further enhance the capabilities of DTI. Further, a bi-exponential [42] analysis fitting the restricted and hindered diffusions separately may be beneficial in characterizing IVOH.

DTI has great potential to provide us with information about tissue microstructure. Every limitation, be it the gradient field strength, design of the appropriate pulse sequence or post processing, when overcome, will continue to improve the performance of the method in order to provide insight into the intricacies of the human mind.

REFERENCES

[1] Alexander, A., Hasan, K., Lazar, M., Tsuruda, J., and Parker, D., "Analysis of partial volume effects in diffusion-tensor MRI," *Magnetic resonance in Medicine*, vol. 45, pp. 770–780, Apr. 2001.

[2] Alexander, A. L., Hasan, K., Kindlmann, G., Parker, D., and Tsuruda, J., "A geometric analysis of diffusion tensor measurements of the human brain," *Magnetic Resonance in Medicine*, vol. 44, pp. 283–291, Aug 2000.

[3] Assaf, Y. and Basser, P., "Composite hindered and restricted model of diffusion (charmed) MR imaging of the human brain," *NeuroImage*, vol. 27, pp. 48–58, Aug. 2005.

[4] Assaf, Y., Freidlin, R., Rohde, G., and Basser3, P., "New modeling and experimental framework to characterize hindered and restricted water diffusion in brain white matter," *Magnetic Resonance in Medicine*, vol. 52, pp. 965–978, Nov. 2004.

[5] Assaf, Y., Mayk, A., and Cohen, Y., "Displacement imaging of spinal cord using q-space diffusion-weighted MRI," *Magnetic Resonance in Medicine*, vol. 44, pp. 713–722, Oct. 2000.

[6] Bammer, R., "Basics of diffusion-weighted imaging," *European Journal of Radiology*, vol. 45, pp. 169–184, Mar. 2002.

[7] Bashat, D., Sera, L., Graif, M., Panika, P., Hender, T., Cohen, Y., and Assaf, Y., "Normal white matter development from infancy to adulthood: Comparing diffusion tensor and high b value diffusion weighted MR images," *Journal of Magnetic Resonance Imaging*, vol. 21, pp. 503 – 511, May 2005.

[8] Basser, P. and Pierpaoli, C., "Microstructural and physiological features of tissues elucidated by quantitative-diffusion tensor MRI," *Journal of Magnetic Resonance B*, vol. 111, pp. 209–219, Jun 1996.

[9] Büchel, C., Raedler, T., Sommer, M., Sach, M., Weiller, C., and Koch, M., "White matter asymmetry in the human brain: A diffusion tensor MRI study," *Cerebral Cortex*, vol. 14, pp. 945–951, Sept. 2004.

[10] Bealieu, C., "The basis of anisotropic water diffusion in the nervous system - a technical review," *Nuclear Magnetic Resonance in Biomedicine*, vol. 15, pp. 435–455, Dec. 2002.

[11] Beaulieu, C., Does, M., Snyder, R., and Allen, P., "Changes in water diffusion due to wallerian degeneration in peripheral nerve," *Magnetic Resonance in Medicine*, vol. 36, pp. 627–634, Oct. 1996.

[12] Bhagat, Y. and Beaulieu, C., "Diffusion anisotropy in subcortical white matter and the cortical gray matter: Changes with aging and the role of CSF-suppression," *Journal of Magnetic Resonance Imaging*, vol. 20, pp. 216–227, Aug. 2004.

[13] D'Arceuil, H. and A.Crespigny, "The effects of brain tissue decomposition on diffusion tensor imaging and tractography," *NeuroImage*, vol. 36, pp. 64–68, May 2007.

[14] D'Arceuil, H., Westmoreland, S., and Crespigny, A., "An approach to high resolution diffusion tensor imaging in fixed primate brain," *NeuroImage*, vol. 35, pp. 553–565, Jan. 2007.

[15] Dardzinski, K. H. B. and Sotak, C., "The application of porous-media theory to the investigation of time-dependent diffusion in in vivo systems," *NMR Biomed.*, vol. 8, pp. 297–306, Dec. 1995.

[16] Duong, T., Sehy, J., Yablonskiy, D., Snider, B., Ackerman, J., and Neil, J., "Extracellular apparent diffusion in rat brain," *Magnetic Resonance in Medicine*, vol. 45, pp. 801–810, Apr. 2001.

[17] Einstein, A., *Investigation on the theory of the Brownian movement.* New York: Dover, 1926.

[18] Falk, D., Froese, N., Sade, D., and Dudek, B., "Sex difference in brain/body relationship of monkeys and humans," *Journal of Human Evolution*, vol. 36, pp. 233–238, Feb. 1992.

[19] Felleman, D. and Essen, D. V., "Distributed hierarchical processing in the primate cerebral cortex," *Cerebral Cortex*, vol. 11, pp. 482–495, Jan. 1991.

[20] Foong, J., Maier, M., Clark, C., Barker, G., Miller, D., and Ron, M., "Neuropathologica abnormalities of the copus callosum in schizophrenia: A diffusion tensor imaging study," *Journal of Neurology, Neurosurgery and Psychiatry*, vol. 68, pp. 242–244, Feb. 2000.

[21] Gray, H., *Anatomy of the Human Body.* New York: bartleby.com, Last Accessed: May 12, 2009, 2000.

[22] Gullmar, D., Hauesien, J., and Reichenbach, J., "Analysis of b-value calculations in diffusion weighted and diffusion tensor imaging," *Concepts in Magnetic Resonance Part A*, vol. 25A, p. 53:66, Mar. 2004.

[23] Hahn, E., "Spin echoes," *Physics Review*, vol. 80, pp. 580–594, Nov. 1950.

[24] Hasan, K., Alexander, A., and Narayana, P., "Does fractional anisotropy have better noise immunity characteristics than relative anisotropy in diffusion tensor MRI," *Magnetic Resonance in Medicine*, vol. 51, pp. 413–417, Feb 2004.

[25] Hines, A. and Maddox, R., *Mass Transfer: Fundamentals and Applications*. Prentice Hall International Series in the Physical and Chemical Engineering Sciences, New Jersey: Prentice-Hall, 1985.

[26] Horsfield, M., Barker, G., and McDonald, W., "Self-diffusion in CNS tissue by volume-selective proton NMR," *Magnetic Resonance in Medicine*, vol. 31, pp. 637–644, June 1994.

[27] Jeffery, G., "Architecture of the optic chiasm and the mechanisms that sculpt its development," *Physiological Review*, vol. 81, pp. 1393–1414, Oct. 2001.

[28] Jiang, H., van Zijl, P., Kim, J., Pearlson, G., and Mori, S., "DtiStudio: Resource program for diffusion tensor computation and fiber bundle tracking," *Computer Methods and Programs in Biomedicine*, vol. 81, pp. 106–116, Jan. 2006.

[29] Kaas, J. and Huerta, M., *The Subcortical Visual System of Primates*. New York: A.R. Liss, 1986.

[30] Kaas, J., Huerta, M., Weber, J., and Harting, J., "Patterns of retinal terminations and laminar organization of the lateral geniculate nucleus of primates," *The Journal of Comparative Neurology*, vol. 182, pp. 517–553, Dec. 1978.

[31] Kandel, E., Schwartz, J., and Jessell, T., *Principles on Neural Science*. United States: McGraw Hill, 1.

[32] Kim, M., Ronen, I., Ugurbil, K., and Kim, D., "Spatial resolution dependence of DTI tractography in human occipito-callosal region," *NeuroImage*, vol. 32, pp. 1243–1249, Sept. 2006.

[33] Kim, S., Chi-Fishman, G., Barnett, A., and Pierpaoli, C., "Dependence on diffusion time of apparent diffusion tensor of *ex vivo* calf tongue and heart," *Magnetic Resonance in Medicine*, vol. 54, pp. 1387–1396, Nov. 2005.

[34] Kubicki, M., Park, H., Westin, C., Nestor, P., Mulkern, R., Maier, S., Niznikiewicz, M., E.E. Connor and, J. L., Frumin, M., Kikinis, R., Jolesz, F., McCarley, R., and Shenton, M., "DTI and MTR abnormalities in schizophrenia: Analysis of white matter integrity," *NeuroImage*, vol. 26, pp. 1109–1118, July 2005.

[35] LeBihan, D., Breton, E., Lallemand, D., Grenier, P., Cabanis, E., and Laval-Jeantet, M., "MR imaging of intravoxel incoherent motions: Application to diffusion and perfusion in neurologic disorders," *Radiology*, vol. 161, pp. 401–407, Nov. 1986.

[36] LeBihan, D., Turner, R., and Douek, P., "Is water diffusion restricted in human white matter? an echo-planar NMR imaging study," *Neuroreprt*, vol. 4, pp. 887–890, July 1993.

[37] Lin, C., Tseng, W., Cheng, H., and Chen, J., "Validation of diffusion tensor magnetic resonance axonal fiber imaging with registered manganese-enhanced optic tracts," *NeuroImage*, vol. 14, pp. 1035–1047, Jan. 2001.

[38] Lin, C., Weeden, V., Chen, J., Yao, C., and Tseng, W., "Validation of diffusion spectrum manetic resonance imaging with manganese enhanced rat optic tracts and *Ex Vivo* phantoms," *NeuroImage*, vol. 19, pp. 482–495, Mar. 2003.

[39] Liu, C., Bammer, R., Acar, B., and Moseley, M., "Characterizing non-gaussian diffusion by using generalized diffusion tensors," *Magnetic Resonance in Medicine*, vol. 51, pp. 924–937, Dec. 2004.

[40] Liu, C., Bammer, R., and Moseley, M., "Generalized diffusion tensor imaging (GDTI): a method for characterizing and imaging diffusion anisotropy caused by non-gaussian diffusion," *Israel Journal of Chemistry*, vol. 43, pp. 145–154, Dec. 2003.

[41] Lorenz, R., Kreher, B., Hennig, J., Bellemann, M., and Ilyasov, K., "Anisotropic fiber phantom for DTI validation on a clinical scanner," tech. rep., International Society for Magnetic Resonance in Medicine, Seattle, USA, June 2006.

[42] Maier, S., Vajapeyam, S., Mamata, H., Westin, C.-F., Jolesz, F., and Mulkern, R. V., "Biexponential diffusion tensor analysis of human brain diffusion data," *Manetic Resonance in Medicine*, vol. 51, pp. 321–330, Feb. 2004.

[43] Mamata, H., Jolesz, F., and Maier, S., "Characterization of central nervous system structures by magnetic resonance diffusion anisotropy," *Neurochemistry International*, vol. 45, pp. 553–560, Sept. 2004.

[44] Masutani, Y., *A New PC-based* MR *Diffusion Tensor Analysis System for Learning and Diagnosing Brain White Matter Tracts*. InfoRAD, Chicago, Radiological Society of North America, 2002.

[45] Mattiello, J., Basser, P., and LeBihan, D., "The b-matrix in diffusion tensor echo planar imaging," *Magnetic Resonance in Medicine*, vol. 37, pp. 292–300, Dec. 1997.

[46] Merboldt, K.-D., Hanicke, W., Bruhn, H., Gyngell, M. L., and Frahm, J., "Diffusion imaging of the human brain *in vivo* using high-speed STEAM MRI," *Magnetic Resonance in Medicine*, vol. 23, pp. 179–192, Nov. 1992.

[47] Milner, R., *Cranial Capacity.* The Encyclopedia of Evolution: Humanity's Eearch for Its Origin, New York: Holt, 1990.

[48] Mori, S., Crain, B., Chacko, V., and van Zijl, P., "Three dimensional tracking of the axonal projections in the brain by magnetic resonance imaging," *Annals of Neurology*, vol. 45, pp. 265–269, Feb. 1999.

[49] Mori, S. and van Zijl, P., "Fiber tracking: Principles and strategies - a technical review," *Nuclear Megnetic Resonance in Biomedicine*, vol. 15, pp. 468–480, Nov. 2002.

[50] Moseley, M., "Diffusion tensor imaging and aging - a review," *Nuclear Magnetic Resonance in Biomedicine*, vol. 15, pp. 553–560, Nov. 2002.

[51] Mukherjee, P., Miller, J., Shimony, J., Philip, J., Nehra, D., Snyder, A., Conturo, T., Neil, J., and McKinstry, R., "Diffusion-tensor MR imaging of gray and white matter development during normal human brain maturation," *American Journal of Neuroradiology*, vol. 23, pp. 1445–1456, Oct. 2002.

[52] Mulkern, R., Gudbjartsson, H., Westin, C.-F., Zengingonul, H., Gartner, W., Guttmann, C., Robertson, R., Kyriakos, W., R. Schwartz, D. Holtzman, F. J., and Maier, S., "Multi-component apparent diffusion coefficients in human brain," *Nuclear Magnetic Resonance in Biomedicine*, vol. 12, pp. 51–62, Mar. 1999.

[53] Naggaraa, O., Oppenheima, C., Rieub, D., N. Raouxb, S. Rodrigoa, G. D.-B., and Medera, J., "Diffusion tensor imaging in early alzheimer's disease," *Psychiatry Research: Neuroimaging*, vol. 146, pp. 243–249, Jan. 2006.

[54] Nair, G., Tanahashi, Y., Low, H., Billing-Gagliardi, S., Schwartz, W., and Duong, T., "Myelination and long diffusion time alter diffusion-tensor imaging contrast in myelin-deficient *shiverer* mice," *NeuroImage*, vol. 28, pp. 165–174, July 2005.

[55] Neeman, M., Freyer, J., and Sillerud, L., "A simple method of obtaining cross-term-free images for diffusion anisotropy studies in NMR microcimaging," *Magnetic Resonance in Medicine*, vol. 21, p. 138:143, Nov. 1991.

[56] Neuvonen, T. and Salli, E., "characterizating diffusion tensor imaging data with directional entropy," *Proceedings of Institute of Electrical and Electronic Engineering in Medicine and Biology, 27th Annual Conference, Shanghai, China*, pp. 5798–5801, Sept. 2005.

[57] Ozarslan, E. and Mareci, T., "Generalized diffusion tensor imaging and analytical relationships between diffusion tensor imaging and high angular resolution diffusion imaging," *Magnetic Resonance in Medicine*, vol. 50, pp. 955–965, Nov 2003.

[58] Papadopoulos, M., Kim, J., and Verkman, A., "Extracellular space diffusion in central nervous system: Anisotropic diffusion measured by elliptical surface photobleaching," *Biophysics Journal*, vol. 89, pp. 3660–3668, Nov. 2005.

[59] Parker, G., Wheeler-Kingshott, C., and Barker, G., "Estimating distributed anatomical connectivity using fast marching methods and diffusion tensor imaging," *Magnetic Resonance in Medicine*, vol. 21, pp. 505–512, May 2002.

[60] Parker, G., Stephan, K., Barker, G., Rowe, J., MacManus, D., Wheeler-Kingshott, C., Ciccarelli, O., Passingham, R., Spinks, R., Lemon, R., and Turner, R., "Initial demonstration of in vivo tracing of axonal projections in the macaque brain and comparison with the human brain using diffusion tensor imaging and fast marching tractography," *NeuroImage*, vol. 15, pp. 797–809, Apr. 2002.

[61] Peled, S., "New perspectives on the sources of white matter dti signal," *IEEE Transactions on Medicial Imaging*, vol. 26, pp. 1448–1455, Nov. 2007.

[62] Peled, S., Cory, D., Raymond, S., Kirschner, D., and Jolesz, F., "Water diffusion, T2, and compartmentation in frog sciatic nerve," *Magnetic Resonance in Medicine*, vol. 42, pp. 911–918, Oct. 1999.

[63] Pfefferbaum, A., Sullivan, E., hedehus, M., Lim, K., Adalsteinsson, E., and Moseley, M., "Age-related decline in brain white matter measured with spatially correlated echo-panar diffusion tensor imaging," *Magnetic Resonance in Medicine*, vol. 44, pp. 259–268, July 2000.

[64] Pfefferbaum, A., Sullivanb, E., Adalsteinssonc, E., Garrickd, T., and Harper, C., "Postmortem MR imaging of formalin-fixed human brain," *NeuroImage*, vol. 21, pp. 1585–644, Apr. 2004.

[65] P.J.Basser, Matiello, J., and LeBihan, D., "Estimation of the effective self-diffusion tensor from the NMR spin echo," *Journal of Magnetic Resonance*, vol. 103, pp. 247–254, Mar. 1994.

[66] Reese, T., Heid, O., Weisskoff, R., and Wedeen, V., "Reduction of eddy-current-induced distortion in diffusion MRI using a twice-refocused spin echo," *Magnetic Resonance in Medicine*, vol. 49, pp. 177–182, Dec. 2003.

[67] Rollins, N., "Clinical applications of diffusion tensor imaging and tractography in children," *Pediatric Radiology*, vol. 37, pp. 769–780, June 2007.

[68] Roth, R. and Dicke, U., "Evolution of the brain and intelligence," *TRENDS in Cognitive Sciences*, vol. 9, pp. 250–256, May 2005.

[69] Sotak, C., "The role of diffusion tensor imaging in the evaluation of ischemic brain injury," *Nuclear Magnetic Resonance in Biomedicine*, vol. 15, pp. 561–569, Nov 2002.

[70] Staempfli, P., Jaermann, T., Crelier, G., Kollias, S., Valavanis, A., and Boesiger, P., "Resolving fiber crossing using advanced fast marching tractography based on diffusion tensor imaging," *NeuroImage*, vol. 30, pp. 110–120, Mar. 2006.

[71] Stephan, K., Kamper, L., Bozkurt, A., Burns, G., Young, M., and Kotter, R., "The organization of neural systems in the primate cerebral cortex," *Proceedings of the Royal Society of London. Series B, Biological Sciences*, vol. 252, pp. 13–18, Apr. 1991.

[72] Sun, S.-W., Neil, J., and Song, S., "Relative indices of water diffusion anisotropy are equivalent in live and formalin-fixed mouse brains," *Magnetic Resonance in Medicine*, vol. 50, pp. 743–748, July 2003.

[73] Tanner, J. and Stejskal, E., "Spin diffusion measurements: Spin echoes in the presence of a time-dependent field gradient," *The Journal of Chemical Physics*, vol. 42, pp. 280–292, Jan. 1965.

[74] Teipel, S., Meindl, T., Grinberg, L., Heinsen, H., and Hampel, H., "Novel MRI techniques in the assessment of dementia," *European Journal of Nucear Medicine and Molecular Imaging*, vol. 35, pp. 58–69, Mar. 2008.

[75] Tseng, W. and Kuo, L., "Diffusion magnetic resonance imaging in neuroimaging," tech. rep., Aug. 2008.

[76] Tuch, D., "Q-ball imaging," *Magnetic Resonance in Medicine*, vol. 52, pp. 1358–1372, July 2004.

[77] Tuch, D., Reese, T., Wiegell, M., Makris, N., Belliveau, J., and Wedeen, V., "High angular resolution diffusion imaging reveals intravoxel white matter fiber heterogeneity," *Magnetic Resonance in Medicine*, vol. 48, pp. 577–582, May 2002.

[78] Tuch, D., Wisco, J., Khachaturian, M., Ekstrom, L., R.Kotter, and W.Vanduffel, "Q-ball imaging of macaque white matter architecture," *Philosophical Transactions of the Royal Society B*, vol. 360, pp. 869–879, May 2005.

[79] Vilee, C., *Biology*. Biology, Philadelphia: Saunders, 1954.

[80] Virta, A., Barnett, A., and Pierpaoli, C., "Visualizing and characterizing white matter fiber structure and architecture in the human pyramidal tract using diffusion tensor mri," *Magnetic Resonance Imaging*, vol. 17, pp. 1121–1133, Oct. 1999.

[81] von dem Hagen, E. and Henkelman, R., "Orientational diffusion reflects fiber structure within a voxel," *Magnetic Resonance in Medicine*, vol. 48, pp. 454–459, Sept. 2002.

[82] Werring, D., Clark, C., Parker, G., Miller, D., and Thomson, A., "An direct demonstration of structure and function in the visual system: Combining diffusion tensor imaging with functional magnetic resonance imaging," *NeuroImage*, vol. 9, pp. 352–361, Mar. 1999.

[83] Westin, C., Peled, S., Gudbjartsson, H., Kikinis, R., and Jolesz, F., "Gerometrical diffusion measures for MRI from tensor based analysis," *Annual Proceedings of the* 5_{th} *International Society for Magnetic Resonance in Medicine Conference, Vancouver*, Apr 1997.

[84] Wu, Y. and Alexander, A., "Hybrid diffusion imaging," *NeuroImage*, vol. 36, pp. 617–629, July 2007.

[85] Xu, J., Rasmussen, I.-A., J.Lagopoulos, and Haberg, A., "Diffuse axonal injury in severe traumatic brain injury visualized using high-resolution diffusion tensor imaging," *Journal of Neurotrauma*, vol. 24, pp. 753–765, May 2007.

[86] Xue, R., vanZijl, P., Crain, B., Solaiyappan, M., and Mori, S., "*In vivo* three-dimensional reconstruction of rat brain axonal projections by diffusion tensor imaging," *Manetic Resonance in Medicine*, vol. 42, pp. 1123–1127, Nov. 1999.

[87] Yassine, I., Metwalli, N., Youssef, A., and Kadah, K., "Study of the effect of noise on the calculation of diffusion indices in diffusion tensor magnetic resonance imaging," tech. rep., Cairo International Biomedical Engineering Conference, Cairo, Egypt, Nov. 2004.

[88] Young, M., "The organization of neural systems in the primate cerebral cortex," *Proceedings of the Royal Society of London. Series B, Biological Sciences*, vol. 252, pp. 13–18, Apr. 1991.

[89] Zaraiskaya, T., Kumbhare, D., and Noseworthy, M., "Diffusion tensor imaging in evaluation of human skeletal muscle injury," *Journal of Magnetic Resonance Imaging*, vol. 24, pp. 402–408, Aug. 2006.

[90] Zhang, L., Thomas, K., Davidson, M., Casey, B., Heier, L., and Ulug, A., "MR quantitation of volume and diffusion changes in the developing brain," *American Journal of Neuroradiology*, vol. 26, pp. 45–49, Jan. 2005.

INDEX

VITA

Swati Rane is a graduate student of the Dwight Look College of Engineering at Texas A&M University, Texas. She completed her M.S. degree in Electrical Engineering in August 2005. Her thesis was based on the characterization and comparison of parallel magnetic resonance imaging techniques. Swati earned her B.E. degree in Electronics and Telecommunication from Pune University in August 2003.